

# A 3D Diffusive and Advective Model of Electron Transport Applied to the Pulsar Wind Nebula HESS J1825-137

T. Collins,<sup>1\*</sup>, G. Rowell<sup>1</sup>, S. Einecke<sup>1</sup>, F. Voisin<sup>1</sup>, Y. Fukui<sup>2</sup> and H. Sano<sup>3</sup>

<sup>1</sup>*School of Physical Sciences, University of Adelaide, Adelaide 5005, Australia*

<sup>2</sup>*Department of Physics, University of Nagoya, Furo-cho, Chikusa-ku, Nagoya, 464-8601, Japan*

<sup>3</sup>*Faculty of Engineering, Gifu University, Yanagido 1-1, Gifu, 501-1193, Japan*

Accepted XXX. Received YYY; in original form ZZZ

## ABSTRACT

HESS J1825-137 is one of the most powerful and luminous TeV gamma-ray pulsar wind nebulae (PWNe), making it an excellent laboratory to study particle transportation around pulsars. We present a model of the (diffusive and advective) transport and radiative losses of electrons from the pulsar PSR 1826-1334 powering HESS J1825-137 using interstellar medium gas (ISM) data, soft photon fields and a spatially varying magnetic field. We find that for the characteristic age of 21 kyr, PSR 1826-1334 is unable to meet the energy requirements to match the observed X-ray and gamma-ray emission. An older age of 40 kyr, an energy budget of 14% of the pulsar's spin-down power and advective flow with a velocity of  $v = 0.002c$  towards lower Galactic longitudes are able to produce an asymmetric gamma-ray morphology and the multi-wavelength spectral energy distribution towards HESS J1825-137. A turbulent ISM with magnetic field of  $B = 20 \mu\text{G}$  to  $60 \mu\text{G}$  to the north of HESS J1825-137 (as suggested by ISM observations) is required to prevent significant gamma-ray contamination towards the northern TeV source HESS J1826-130.

**Key words:** cosmic rays - ISM: evolution - gamma-rays: general - X-rays: general - ISM individual (HESS J1825-137) - pulsars: individual (PSR J1826-1334)

## 1 INTRODUCTION

HESS J1825-137 is a luminous pulsar wind nebula (PWN) powered by pulsar PSR 1826-1334 with spin-down power  $\dot{E} = 2.8 \times 10^{36} \text{ erg s}^{-1}$  and characteristic age  $\tau_c = P/2\dot{P} = 21.4 \text{ kyr}$  (Manchester et al. 2005). The distance to PSR J1826-1334 has been estimated to lie at 3.6 kpc based on dispersion measurements (Taylor & Cordes 1993; Cordes & Lazio 2002), however we will use a distance of 4 kpc in line with Van Etten & Romani (2011) and H.E.S.S. Collaboration et al. (2019). The TeV gamma-ray emission from HESS J1825-137 has characteristic  $(1/e)$  radius of  $0.66^\circ \pm 0.03^\circ_{\text{stat}} \pm 0.04^\circ_{\text{sys}}$ , implying a radius of  $\approx 46 \text{ pc}$  based on a distance of 4 kpc (H.E.S.S. Collaboration et al. 2019). Owing to its brightness in TeV gamma rays, HESS J1825-137 is an ideal laboratory to study relativistic particle transport in and around middle-aged PWNe. Several studies (e.g. Porth et al. (2016), Giacinti et al. (2020)) suggest that both diffusive and advective transport mechanisms are required to explain the extended gamma-ray morphology towards PWNe.

Situated  $0.7^\circ$  north of HESS J1825-137 (see Figure 1), HESS J1826-130 is a TeV gamma-ray source and possible accelerator of cosmic rays up to PeV energies (Abeysekara et al. 2020;

Cao et al. 2021). Due to its close proximity to HESS J1825-137, HESS J1826-130 was originally considered an extension of HESS J1825-137 until it revealed it was a separate source of gamma rays (H.E.S.S. Collaboration et al. 2018a; Aharonian et al. 2005). The two nearby supernova remnants (SNRs) SNR G018.1-0.1 and SNR G018.6-0.2 (Odegard 1986; Brogan et al. 2006) were deemed to be unlikely lie to be associated with HESS J1826-137 due to their offset positions and small angular diameters (H.E.S.S. Collaboration et al. 2020). Instead, the Eel PWN (PWN G18.5-0.4) and PSR J1826-1256 are associated with HESS J1826-130 based on spatial coincidence (H.E.S.S. Collaboration et al. 2018a). PSR J1826-1256 has a spin-down power of  $3.6 \times 10^{36} \text{ erg s}^{-1}$  and characteristic age of 14 kyr, well within the range of pulsar properties associated with TeV PWNe (Manchester et al. 2005; H.E.S.S. Collaboration et al. 2018b).

Araya et al. (2019) revealed GeV gamma-ray emission  $\sim 2.5^\circ$  to the Galactic south of HESS J1825-137. The same study postulated that the GeV emission from this region originates from cosmic rays accelerated by the SNR or PWN associated with HESS J1825-137 or a star-forming region such as the Cygnus Cocoon. A comprehensive modelling of spectral energy distributions (SED) towards the GeV region suggests that the emission may be reflective of an earlier epoch of the PWN or a combination of HESS J1825-137 and nearby compact object LS 5039 (Collins et al. 2021).

\* E-mail: tiffany.collins@adelaide.edu.au

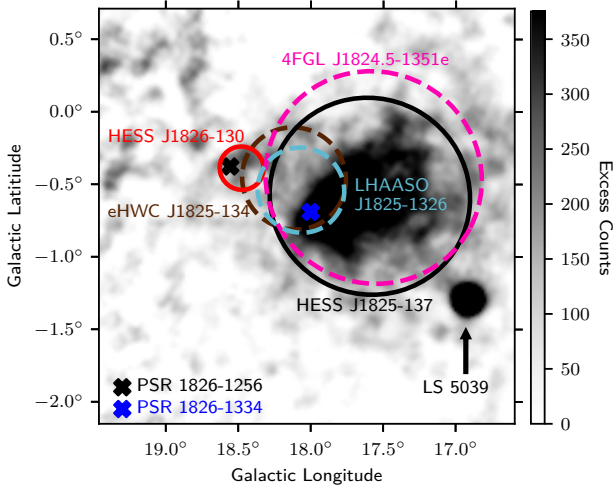


**Figure 1.** HESS excess counts towards HESS J1825-137 (H.E.S.S. Collaboration et al. 2019) overlaid by the regions used to extract the gamma-ray spectra towards HESS J1825-137 (black) and HESS J1826-130 (red). 4FGL J1824.5-1351e, eHWC J1825-134 and LHAASO J1825-1326 are shown by the purple, brown and cyan dashed circles respectively with the positions of PSR J1826-1334 (blue) and PSR J1826-1256 (black). The position of nearby binary system LS 5039 is indicated by the black arrow.

The PWN associated with HESS J1825-137 must be expanding within the progenitor SNR. A large H $\alpha$  rim-like structure discovered by Stupar et al. (2008) is present towards the south of HESS J1825-137. Voisin et al. (2016) postulated a connection between this rim and another southern H $\alpha$  rim and the progenitor SNR of HESS J1825-137. Both structures lie  $\approx 1.7^\circ$  away from PSR 1826-1334 ( $\approx 120$  pc for a distance of 4 kpc), which is consistent with the predicted SNR radius of  $\approx 130$  pc as suggested by de Jager & Djannati-Ataï (2009).

The evolution of the cosmic-ray number density distribution can be described by the Fokker-Planck equation for particle transport (e.g. (Skilling 1975; Cesarsky & Volk 1978)). Henceforth, this equation will be called the transport equation for simplicity. Analytical solutions of the transport equation can be found for specific cases, e.g. an impulsive source in a homogeneous environment (Blumenthal & Gould 1970; Atoyan et al. 1995; Aharonian & Atoyan 1996). However, it can only be solved numerically for more complex systems, e.g. continuous sources where cosmic-ray propagation and radiative losses vary strongly with position.

Many models of HESS J1825-137 and other PWN assume a homogeneous nebula, where high-energy electrons are injected into a symmetric sphere of constant density and magnetic field (e.g. H.E.S.S. Collaboration et al. (2019); Principe et al. (2020)). For example, the work conducted by Van Etten & Romani (2011) treated the transport of electrons from the powering pulsar as a series of uniform, spherical ‘bubbles’ and projected the gamma-ray SED onto a 2D plane. However, the observed asymmetric gamma-ray morphology observed towards HESS J1825-137 suggests a similar irregular electron density and/or magnetic field and therefore requires a more complex model.

In this paper, we present a model that incorporates 3D distributions of the ISM hydrogen number density and magnetic field and that solves the transport equation numerically. This model assumes PSR J1826-1334 to be a source of high-energy electrons and aims at reproducing the X-ray and gamma-ray morphology, SED and surface brightness radial profiles towards HESS J1825-137.

## 2 PARTICLE TRANSPORT AND MULTI-WAVELENGTH EMISSION

Upon the release from an accelerator, such as a SNR or PWN, cosmic-ray rays are transported through the ISM and experience radiative losses. The evolution of the number density distribution of cosmic rays,  $n = n(\gamma, t, \vec{r})$ , with Lorentz factor  $\gamma$ , at position  $\vec{r} = (x, y, z)$  and time  $t$  after the birth of the accelerator, can be described by (e.g. Skilling (1975); Cesarsky & Volk (1978)):

$$\frac{\partial n}{\partial t} = \frac{\partial}{\partial \gamma} (\dot{\gamma} n) + \nabla \cdot (\bar{\bar{D}} \cdot \nabla n) - \nabla \cdot (n \vec{v}_A) - \frac{1}{3} \frac{\partial}{\partial \gamma} (\gamma (\nabla \cdot \vec{v}_A)) n + \frac{\partial}{\partial \gamma} \left( \gamma^2 D_{pp} \frac{\partial}{\partial \gamma} \left( \frac{n}{\gamma^2} \right) \right) + S(\gamma, t, \vec{r}). \quad (1)$$

The first term in Equation 1 gives the evolution of cosmic-ray density due to radiative losses. The second term considers the spatial diffusion of cosmic rays as a second-rank tensor ( $\bar{\bar{D}} = \bar{\bar{D}}(\gamma, t, \vec{r})$ ), allowing preferential direction of transport. The third term describes the evolution of cosmic-ray density due to advection as a co-moving fluid with velocity  $\vec{v}_A = \vec{v}_A(\gamma, t, \vec{r})$ . The fourth term considers losses due to adiabatic expansion. The fifth term represents the re-acceleration of cosmic rays due to stochastic processes with  $D_{pp}$  being the acceleration rate. Finally,  $S(\gamma, t, \vec{r})$  is the cosmic ray source/injection function.

To numerically solve Equation 1, we employ finite difference techniques and discretise a region of interest into a grid of voxels with dimension  $\Delta X \Delta y \Delta z$  and time step  $\Delta t$ :

$$\frac{n(\gamma, t + \Delta t, \vec{r}) - n'(\gamma, t, \vec{r})}{\Delta t} = \left( \frac{\partial n}{\partial t} \right)'_{\text{diff}} + \left( \frac{\partial n}{\partial t} \right)'_{\text{adv}} + \left( \frac{\partial n}{\partial t} \right)'_{\text{adb}} + \left( \frac{\partial n}{\partial t} \right)'_{\text{re-acc}} + S(\gamma, t, \vec{r}), \quad (2)$$

where prime represents the evolution of the number density distribution *after* radiative losses. The subsequent multi-wavelength SED, surface brightness radial profiles and morphology can then be predicted.

The following discussion describes how the implemented model treats individual terms in Equation 2.

### 2.1 Radiation Losses

High-energy electrons interact with the ISM via inverse Compton interactions on ambient photons, via Bremsstrahlung with interstellar gas and via synchrotron interactions against magnetic fields (see Appendix A). The evolution of the electron number density with Lorentz factor  $\gamma$  due to radiative losses is given by:

$$\left( \frac{\partial n}{\partial t} \right)'_{\text{rad}} = \frac{\partial}{\partial \gamma} (\dot{\gamma} n), \quad (3)$$

where  $\dot{\gamma}$  is the cooling rate as given by Manolakou et al. (2007):

$$\dot{\gamma} = b_s \gamma^2 + b_c (3 \ln \gamma + 18.8) + 5.3 b_b + \sum_j b_{IC}^j \gamma^2 F_{KN}^j(\gamma), \quad (4)$$

for the case of ionisation or Bremsstrahlung losses in neutral hydrogen. Here,  $j$  sums over all radiation fields (CMB, infra-red and optical photons),  $b_s$ ,  $b_c$ ,  $b_b$  and  $b_{IC}$  are the coefficients for synchrotron losses, Coulomb losses, Bremsstrahlung losses and inverse

Compton losses respectively and  $F_{\text{KN}}$  is the Klein-Nishina cross section (see Equation A4). The general solution to Equation 3 is:

$$n(\gamma, t + \Delta t) = \frac{\gamma_0}{\gamma} n(\gamma_0, t), \quad (5)$$

with  $\gamma_0 = \gamma + \Delta\gamma$  is the Lorentz factor at time  $t$  before electrons cool to Lorentz factor  $\gamma$  at time  $t + \Delta t$ .

## 2.2 Diffusion

Over distances smaller than the gyro-radius,  $r_g$ , electrons propagate through the ISM via ballistic motion. In a medium with randomised magnetic turbulence ( $\delta B$ ), electrons scatter and the motion switches to a diffusive regime for distances larger than the gyro-radius (e.g. Prosekin et al. (2015)). For a simple case of isotropic diffusion in magnetic field  $B(r)$ , the diffusion tensor in Equation 1 becomes a scalar;  $\overline{D} \rightarrow D(E, B(\vec{r}))$ , where  $E$  is the energy of the cosmic ray.

Suppression of cosmic-ray diffusion is to be expected towards PWNe and SNRs where magnetic field turbulence is enhanced and the diffusion coefficient,  $D(E, B(\vec{r}))$ , can be parameterized by (e.g. Gabici et al. (2007)):

$$D(E, B(\vec{r})) = \chi D_0 \left( \frac{E/\text{TeV}}{B(r)/3 \text{ }\mu\text{G}} \right)^\delta, \quad (6)$$

where  $D_0 = 3 \times 10^{27} \text{ cm}^2 \text{ s}^{-1}$  is the average Galactic diffusion coefficient at 1 GeV,  $\delta = 0.5$  following cosmic-ray observations (e.g. see Strong et al. (2007)) and the diffusion suppression factor,  $\chi$ , takes values  $\leq 1$  depending on the environment (Berezinskii et al. 1990). For example, Gabici et al. (2007) found that highly suppressed diffusion ( $\chi \sim 0.01$ ) in molecular clouds can significantly effect the shape of the observed gamma-ray spectrum. However, the diffusion suppression factor is not well constrained and a variety of  $\chi$  have been found, e.g. Li & Chen (2010), Giuliani et al. (2010) and Gabici et al. (2010) found  $\chi = 0.1, 0.01$  and  $0.06$  towards SNR W28 respectively. Similarly, Protheroe et al. (2008) showed that the suppression factor towards the star-forming region Sgr B2 takes values  $< 0.02$  based on the radio synchrotron flux.

Assuming isotropic homogeneous diffusion, the diffusive component of Equation 2 is given by Equation 7:

$$\left( \frac{\partial n}{\partial t} \right)_{\text{diff}} = \sum_{i=x,y,z} \mathcal{D} \left( n_{i+\Delta i}^t - n_i^t \right) + \mathcal{D} \left( n_{i-\Delta i}^t - n_i^t \right), \quad (7)$$

where electrons from the current time step,  $n(\gamma, t)$ , are first allowed to radiatively cool and are then incremented with the net transfer of electrons from the surrounding voxels.  $\gamma + \Delta\gamma$  describes the Lorentz factor at time  $t$  before electrons cool to factor  $\gamma$  at time  $t + \Delta t$  and  $\mathcal{D} = D(\gamma, B(\vec{r}))/\Delta i^2$  with  $D(\gamma, B(\vec{r}))$  being the diffusion coefficient from Equation 6.

The finite difference technique used in Equation 7 only considers the transport of electrons to/from the surrounding voxels. If the time step is large enough to allow electrons to travel across more than one voxel, electrons are lost from the system and the finite difference technique is said to be numerically ‘unstable’. Using Von Neuman stability analysis (e.g. see Isaacson (1966)), Equation 7 is stable when:

$$\Delta t \leq \frac{\Delta i^2}{2\Delta t \mathcal{D}_{\text{max}}}. \quad (8)$$

## 2.3 Advection

For simplicity, the velocity due to the bulk flow of electrons ( $\vec{v}_A$ ) was assumed to be spatially and energy independent across the region of interest. Using finite difference techniques, the advective component of Equation 2 is given by Equation 9:

$$\left( \frac{\partial n}{\partial t} \right)_{\text{adv}} = - \sum_{i=x,y,z} v_{A,i} \frac{\Delta t}{\Delta i} \begin{cases} \left( n_{i+\Delta i}^t - n_i^t \right), & v_{A,i} < 0 \\ \left( n_i^t - n_{i-\Delta i}^t \right), & v_{A,i} > 0 \end{cases}, \quad (9)$$

where  $v_{A,i}$  is the component of advective velocity in the  $i$ th direction. Equation 9 uses the forward difference method to approximate the derivative in Equation 2 when  $v_{A,i} < 0$  and the backward difference method when  $v_{A,i} > 0$ . Note that anisotropic diffusion can be approximated by isotropic diffusion plus advection.

For Equation 9 to numerically model the transport of electrons due to advection, the time step must be chosen so that an electron does not travel across more than one voxel in time  $\Delta t$ :

$$\Delta i \geq |v_{A,i}| \Delta t. \quad (10)$$

## 2.4 Adiabatic expansion and re-acceleration of electrons

For an energy-independent advective velocity  $\vec{v}_A$ , losses due to adiabatic expansion is given by:

$$\left( \frac{\partial n}{\partial t} \right)_{\text{adb}} = -\frac{1}{3} (\nabla \cdot \vec{v}_A) n. \quad (11)$$

Studies, such as Tanaka & Takahara (2010) and Porth et al. (2016) which considered spherically symmetric advection, concluded that adiabatic losses are dominant over radiation losses for low-energy electrons ( $< 10 \text{ TeV}$ ). Therefore, losses due to adiabatic expansion are not considered here but are left for future work.

The termination shock (TS) of pulsars has been proposed as sites for re-acceleration of electrons through diffusive shock acceleration (DSA). By ensuring the voxel size ( $\Delta x, \Delta y, \Delta z$ ) is larger than the diameter of the termination shock (0.2 pc, (Gaensler & Slane 2006)), electrons are both injected and re-accelerated within the same voxel. Therefore, the source term in Equation 2 treats the injected electron spectra as the spectra obtained after re-acceleration due to the TS. Furthermore, magnetohydrodynamic models (e.g. Lemoine & Pelletier (2010); Sironi et al. (2015)) suggest that DSA at the TS is too suppressed for electron acceleration up to energies responsible for the TeV emission seen towards PWNe. Hence, the re-acceleration of electrons is left for future work.

## 2.5 Multi-wavelength photon production

The final electron number density distribution around the pulsar is obtained by solving Equation 2 in discrete time steps  $\Delta t$  until the desired age is reached. The subsequent photon SED emitted by each voxel is calculated and summed along the line of sight ( $z$ ). Appendix A gives further details of the SED contribution for inverse Compton, Bremsstrahlung and synchrotron interactions.

## 3 APPLICATION TO HESS J1825-137

The modelling described in section 2 was then applied to the PWN HESS J1825-137 with the pulsar PSR J1826-1334 being the accelerator of high-energy electrons. PSR J1826-1334 is located at  $\ell = 18^\circ$

$b = -0.69^\circ$  and has a proper motion of  $\approx 440 \text{ km s}^{-1}$  (assuming a distance of 4 kpc) approximately perpendicular to the extended TeV emission (see Figure 3) (Manchester et al. 2005). Hence, the proper motion of the pulsar is unlikely to be related to the asymmetric emission and our model will assume that electrons are injected at the current position of the pulsar for simplicity. Two different ages of PSR J1826-1334 were considered, the characteristic age of 21.4 kyr and the older age of 40 kyr suggested by Van Etten & Romani (2011).

Each voxel in the 3D grid has a volume of  $\Delta x \Delta y \Delta z$  where  $\Delta z$  is the voxel length in the line of sight and  $\Delta x$  and  $\Delta y$  are the voxel length along Galactic longitude and latitude respectively. For the purposes of this study, we utilised a  $200 \text{ pc} \times 200 \text{ pc} \times 200 \text{ pc}$  grid consisting of voxels of size  $2 \text{ pc} \times 2 \text{ pc} \times 2 \text{ pc}$  ( $\approx 0.03^\circ \times 0.03^\circ \times 0.03^\circ$ ). The pulsar was located in the centre of the grid at  $(0, 0, 0)$  with the  $z = (0 \pm 1)$  slice lying at distance 4.0 kpc. The time step used for the finite difference technique is  $\approx 8 \text{ yr}$ .

### 3.1 Electron injection

High energy electrons are injected into the 3D grid and follow an exponential cutoff power-law:

$$S(E, t) = A \left( \frac{E}{1 \text{ TeV}} \right)^{-\Gamma} \exp \left( -\frac{E}{E_c} \right), \quad (12)$$

where  $E_c$  is the cutoff energy and  $A$  is the normalisation factor such that:

$$L_{\text{inj}}(t) = \int_{E_{\text{min}}}^{E_{\text{max}}} S(E, t) dE, \quad (13)$$

with  $L_{\text{inj}} = \eta \dot{E}$  being the electron injection luminosity,  $\eta < 1$  is the conversion efficiency of the pulsar spin-down power,  $E_{\text{min}} = 10^{-6} \text{ TeV}$  and  $E_{\text{max}} = 500 \text{ TeV}$ . The spin-down power,  $\dot{E}(t)$  at time  $t$  is given by (Haensel et al. 2007):

$$\dot{E}(t) = \dot{E}(t = t_{\text{age}}) \left[ 1 + (n - 1) \frac{\dot{P}(t - t_{\text{age}})}{P} \right]^{-\Gamma_n}, \quad (14)$$

where  $n$  is the braking index of the pulsar,  $\Gamma_n = (n + 1)/(n - 1)$  and  $\dot{E}(t = t_{\text{age}})$ ,  $P$  and  $\dot{P}$  are the spin-down power, period and spin-down period of the pulsar at the current age  $t_{\text{age}}$ .

## 3.2 The environment towards HESS J1825-137

### 3.2.1 Magnetic Field

Following Van Etten & Romani (2011), the magnetic field due to the PWN was assumed to follow a time-independent power-law with a decreasing magnetic field strength varying with distance  $r$  from the pulsar:

$$B_{\text{PWN}}(r) = B_0 \left( \frac{r}{r_{\text{ts}}} \right)^{-\beta}, \quad (15)$$

where  $r_{\text{ts}} = 0.03 \text{ pc}$  is the radius of the termination shock, and  $B_0$  and  $\beta$  are free parameters optimised to match the multi-wavelength SED of HESS J1825-137. Van Etten & Romani (2011) suggest  $\beta = -0.69$  and  $B_0 = 400 \mu\text{G}$  for an age of 40 kyr. Note that Van Etten & Romani (2011) considers an additional dependence on the spin-down energy of the pulsar which is not considered in this study for simplicity.

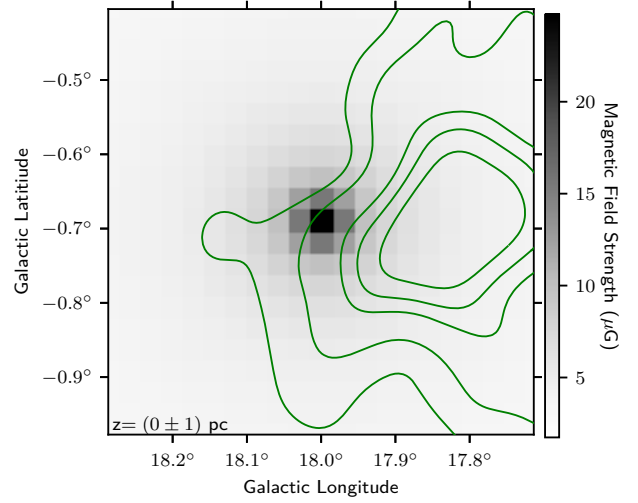


**Figure 2.** The radially symmetric magnetic field due to the pulsar at slice  $z = (0 \pm 1) \text{ pc}$ . Overlaid are the green H.E.S.S. contours at 4, 5, 6, 7, 8 and  $9\sigma$  (H.E.S.S. Collaboration et al. 2019).

### 3.2.2 Interstellar medium

Using the Nanten  $^{12}\text{CO}(1-0)$  survey (Mizuno & Fukui 2004), the total column density of molecular hydrogen,  $N_{\text{H}_2}$ , was traced towards the region of interest using

$$N_{\text{H}_2} = X_{12\text{CO}} W_{12\text{CO}} \quad (16)$$

where  $W_{12\text{CO}}$  is the integrated intensity of the gas.  $X_{12\text{CO}} = 1.5 \times 10^{20} \text{ cm}^{-2} \text{ K}^{-1} \text{ km}^{-1} \text{ s}$  is assumed to be constant over the Galactic plane but may vary with galactocentric radius (1.3 – 1.5 per kpc) (Strong et al. 2004). The size of the 3D grid ( $< 1 \text{ kpc}$ ) allows the assumption of a constant  $X_{12\text{CO}}$  towards the region of interest. PSR 1826-1334 has a dispersion measure distance of 4 kpc, corresponding to a velocity of  $50 \text{ km s}^{-1}$  using the Galactic Rotation model (Brand & Blitz 1993). As there may be local motion of the gas unrelated to Galactic rotation, we consider a velocity range of  $40 - 60 \text{ km s}^{-1}$  (3.5 kpc to 4.5 kpc) consistent with Voisin et al. (2016). Atomic hydrogen in the same velocity range contributes less than 1% to the total column density towards HESS J1825-137 and thus was not considered (Voisin et al. 2016; Collins et al. 2021).

Assuming that all the gas in the  $40 - 60 \text{ km s}^{-1}$  velocity range lies within the 3D grid and the density along the line of sight is constant, the number density of a voxel with column density  $N_{\text{H}_2}$  is given by:

$$n_{\text{H}} = \frac{N_{\text{H}}}{200 \text{ pc}}, \quad (17)$$

where  $N_{\text{H}} = 2.8 N_{\text{H}_2}$  considers a 20% He component.

Stellar winds from the progenitor star of PSR J1826-1334 will push out gas in the nearby vicinity (Castor et al. 1975). The subsequent supernova explosion creates a ‘bubble’ of hot dense gas around a low-density interior. A region of low density gas in the  $40 - 60 \text{ km s}^{-1}$  velocity range can be seen towards the centre of the TeV emission in Figure 3. To include this, any voxels lying within the extent of the PWN volume (a sphere centered on the pulsar with radius  $0.5^\circ$ ) was set to a density of  $0.5 \text{ cm}^{-3}$  based on the average densities expected within massive stellar wind bubbles (Weaver et al. 1977). The Nanten  $^{12}\text{CO}(1-0)$  integrated intensity

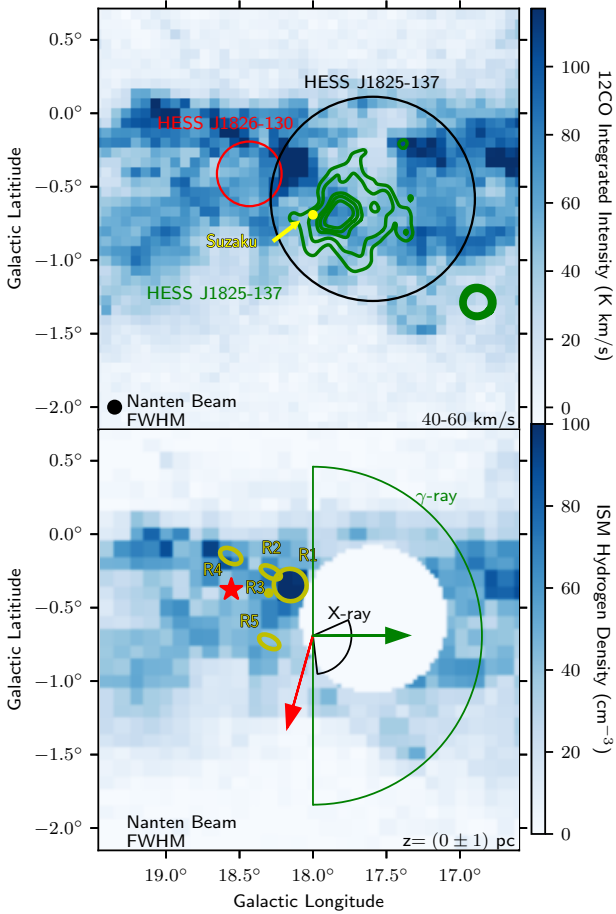


**Figure 3.** (top) Nanten  $^{12}\text{CO}(1-0)$  integrated intensity in the velocity range  $40 - 60 \text{ km s}^{-1}$  corresponding to  $3.5 - 4.5 \text{ kpc}$  overlaid by green H.E.S.S. contours (at 4, 5, 6, 7, 8 and  $9\sigma$ ). The yellow dot represents the Suzaku region A as defined in Uchiyama et al. (2009) and is used to extract the X-ray SED. The region used to obtain the gamma-ray spectra towards HESS J1825-137 and HESS J1826-130 are shown in black and red respectively. (bottom) Calculated ISM number density across the 3D grid at  $z = (0 \pm 1) \text{ pc}$  where the voxels within the PWN extent ( $R < 0.5^\circ$ ) are set to a density of  $0.5 \text{ cm}^{-3}$  to represent the bubble that has been swept out by the stellar wind from the progenitor star. The proper motion of the pulsar is shown by the red arrow with the projected birthplaces for ages 21 kyr and 40 kyr indicated by the green and black dot respectively. The direction of advective particle transport suggested by H.E.S.S. Collaboration et al. (2019) is shown by the green arrow. The black and green segments represent the regions used to extract the X-ray and gamma-ray surface brightness radial profile respectively. Molecular clouds R1-R5 from Voisin et al. (2016) are shown in yellow with the position of PSR J1826-1256 indicated by the red star.

between  $40 - 60 \text{ km s}^{-1}$  and calculated ISM number density at  $z = (0 \pm 1) \text{ pc}$  can be seen in Figure 3.

Turbulent motion in ISM results in an amplification of the magnetic field, suppressing the diffusion of electrons as they travel through the ISM as given by Equation 6. Figure 6 of Voisin et al. (2016) shows a three-coloured image of the CS(1-0) and  $\text{NH}_3$  integrated intensity between  $40 - 60 \text{ km s}^{-1}$  and the  $\text{H}62\alpha$  integrated intensity between  $45 - 65 \text{ km s}^{-1}$  towards the cloud defined as R1 (see Figure 3 for the position of clouds R1-R5 from Voisin et al. (2016)). Located between HESS J1825-137 and HESS J1826-130, cloud R1 is highly turbulent with minimum magnetic field strength of  $21 \mu\text{G}$  as given by Crutcher’s relation (see Equation B1). Given the likely

physical proximity of this turbulent ISM to HESS J1825-137, cloud R1 may act as a barrier for electrons escaping into HESS J1826-130 from PSR 1826-1334 (Voisin et al. 2016).

### 3.2.3 Soft Photon Fields

The photon fields around HESS J1825-137 are estimated utilising the radiation field model described by Popescu et al. (2017); the far-infrared field (FIR) with temperature  $T = 40 \text{ K}$  and energy density  $U = 1 \text{ eV cm}^{-3}$ , near infra-red field (NIR) with temperature  $T = 500 \text{ K}$  and energy density  $0.4 \text{ eV cm}^{-3}$  and optical light with temperature  $T = 3500 \text{ K}$  and energy density of  $U = 1.9 \text{ eV cm}^{-3}$ .

## 3.3 Multi-wavelength Observations

The modelled gamma-ray SED of HESS J1825-137 was matched to the TeV gamma-ray energy flux presented by H.E.S.S. Collaboration et al. (2019) and the GeV spectra from the 4FGL catalogue (Abdollahi et al. 2020). To compare the modelled surface brightness radial profile to Fig. 6 from H.E.S.S. Collaboration et al. (2019), a collection area of  $0.25 \text{ km}^2$  (Benbow 2005) and observation time of 387 hr was used. The X-ray SED and surface brightness radial profile was matched to the results presented by Uchiyama et al. (2009) using a collection area of  $0.029 \text{ m}^2$ .

To investigate the gamma-ray contamination of HESS J1826-130, by HESS J1825-137, we utilised the gamma-ray SED presented by H.E.S.S. Collaboration et al. (2020) and the spectra from the 4FGL catalogue (Abdollahi et al. 2020). H.E.S.S. Collaboration et al. (2020) estimated that the gamma-ray contamination to be  $\approx 40\%$  for photon energies below  $1.5 \text{ TeV}$  and  $20\%$  above  $1.5 \text{ TeV}$ . The modelled X-ray emission towards HESS J1826-130 was constrained by the ROSAT X-ray upper limit calculated using the ROSAT X-ray background tool (Sabot & Snowden 2019).

The regions used to extract the X-ray and gamma-ray SED towards HESS J1825-137 and HESS J1826-130 are shown in Figure 3.

## 3.4 Results

The full list of model parameters can be seen in Table 1, including any constraints based on measurements. A computationally quick single-zone model was utilised to gain insight into the input parameter space towards HESS J1825-137. A single-zone model takes a spherical voxel of uniform ISM to calculate the electron number density distribution due to diffusive and radiative losses. The results of the single-zone modelling are summarised in Appendix. C. For an age of 21 kyr, the single-zone model required electrons to follow an exponential cutoff power-law with spectral index  $\Gamma = 2.1$  and cutoff  $E_c = 40 \text{ TeV}$  to match the gamma-ray SED while an older age of 40 kyr required index of  $\Gamma = 2.1$  and cutoff  $E_c = 50 \text{ TeV}$ .

This section presents three applications of our model towards HESS J1825-137. All models incorporated a simple assumption of isotropic diffusion and radiative losses described in subsection 2.2. Model 1 considered both ages of PSR J1826-1334, 21 kyr and 40 kyr. Model 2 introduced an additional advective component to Model 1 with velocity  $\vec{V}_A = (V_A, 0, 0)$  as suggested by H.E.S.S. Collaboration et al. (2019) to explain the asymmetric gamma-ray morphology. H.E.S.S. Collaboration et al. (2019) constrained the total flow velocity to be  $< 0.01c$ . Model 3 expanded on Model 2 by including turbulent ISM towards HESS J1826-130 (see § 3.2.2)

**Table 1.** Model parameters used for the application towards HESS J1825-137. Fixed parameters refer to those constrained by measurements and non-fixed refers to those that are optimised to observations discussed in subsection 3.3.

Fixed Parameters	Value	Reference
$t$	21 kyr & 40 kyr	a, b
$d$	4 kpc	a
$P$	101 ms	a
$\dot{P}$	$7.5 \times 10^{-14} \text{ s s}^{-1}$	a
$\dot{E}$	$2.8 \times 10^{36} \text{ erg s}^{-1}$	a
$\Delta x, \Delta y, \Delta z$	2 pc	
$\Delta t$	8 yr	
$E_{\min}$	$10^{-6} \text{ TeV}$	
$E_{\max}$	500 TeV	
$D_0$	$3 \times 10^{27} \text{ cm}^2 \text{ s}^{-1}$	c
$r_{\text{ts}}$	0.03 pc	
$U_{\text{CMB}}, T_{\text{CMB}}$	0.26 eV $\text{cm}^{-3}$ , 2.72 K	e
$U_{\text{NIR}}, T_{\text{NIR}}$	1 eV $\text{cm}^{-3}$ , 500 K	e
$U_{\text{FIR}}, T_{\text{FIR}}$	0.4 eV $\text{cm}^{-3}$ , 40 K	e
$U_{\text{Opt}}, T_{\text{Opt}}$	1.9 eV $\text{cm}^{-3}$ , 3500 K	e
Non-fixed Parameters	Value	Reference
$\eta$	$< 1$	
$\chi$	$< 1$	c
$\Gamma$	-	
$E_c$	-	
$B_0$	-	
$\beta$	-	
$n$	2-3	
$\vec{V}_A = (\ell, b, z)$	( $< 0.01c, 0, 0$ )	d
$B_{1826}$	★	

★ See § 3.4.3

a. Manchester et al. (2005)

b. Van Etten & Romani (2011)

c. Berezhinskii et al. (1990)

d. H.E.S.S. Collaboration et al. (2019)

e. Popescu et al. (2017)

to reduce the contamination by HESS J1825-137. The modelled parameters were chosen to match the observations discussed in subsection 3.3 with the parameter list shown in Table 1. The parameters we found to match the multi-wavelength SED and morphology are shown in Table 2.

### 3.4.1 Model 1 (21 & 40 kyr) - Isotropic Diffusion

Figure 4 and 5 shows the modelled gamma-ray morphology in different energy bands, the multi-wavelength SED and the 1–9 keV X-ray and 0.1–91 TeV gamma-ray surface brightness radial profiles for the 21 and 40 kyr models respectively as well as corresponding model inputs.

Both ages predicted that the gamma-ray morphology towards HESS J1825-137 is symmetric around the powering pulsar with some gamma-ray contribution  $< 1 \text{ TeV}$  via Bremsstrahlung radiation toward the region between HESS J1825-137 and HESS J1826-130 (see Figure 4 and Figure 5). The 40 kyr gamma-ray emission between 1–10 TeV extends further from the pulsar than the 21 kyr emission. Both ages predicted a steep surface brightness radial profile for X-rays between 1–9 keV (see the left bottom-middle right panels of Figure 4 and Figure 5). The 21 kyr model was able to replicate the HESS surface brightness radial profile for gamma rays between 0.133–91 TeV (see the bottom-middle right panel of Figure 4) while the 40 kyr model over-predicted the gamma-ray emission for distances  $> 0.5^\circ$  from the pulsar (see the bottom-middle right panel of Figure 5).

The 21 kyr modelled gamma-ray SED predicted by the multi-

zone model was able to match observations with a slight over-prediction ( $\sim 94\%$ ) of the HESS data between 1–10 TeV. While able to predict the normalisation of X-rays produced by synchrotron emission, the model was unable to replicate the slope of the observed Suzaku SED. The multi-zone 40 kyr SED was able to predict both the X-ray and gamma-ray SED with a similar over-prediction in 1–10 TeV photons as seen in the 21 kyr model. A slight ‘bump’ is present in the SED for photons around 50–100 TeV for both ages.

The 21 kyr model required electrons with spectral index  $\Gamma = 2.0$  and cutoff 40 TeV to be injected into the ISM with a spin-down conversion factor of 10.4 to match the multi-wavelength SED. The 40 kyr required a conversion factor of 0.14 with a spectral index and cutoff of 1.9 and 500 TeV respectively. As  $\eta < 1$ , Models 2 and 3 only considered an age of 40 kyr.

Figure 6 shows the modelled SED towards HESS J1826-130 due to electrons escaping from HESS J1825-137 for the 40 kyr model. The SED towards HESS J1826-130 as a result of HESS J1825-137 exceeds observations for photons below 2 TeV. In the model, too many low-energy electrons have escaped into the region towards HESS J1826-130 before losing their energy to radiative losses. It is clear that further refinement of the model is required to accurately describe the region surrounding HESS J1825-137.

### 3.4.2 Model 2 - Isotropic Diffusion + Advection

The gamma-ray morphology in Figure 5 shows that Model 1 (40 kyr) did not reproduce the extended TeV gamma-ray morphology towards HESS J1825-137 at lower Galactic longitudes (see the top-middle left panel of Figure 5). Thus, Model 2 introduced an additional advective component as suggested by (H.E.S.S. Collaboration et al. 2019) towards lower Galactic longitudes. See Table 2 for the model parameters.

The modelled flux, surface brightness radial profiles and gamma-ray morphology for Model 2 40 kyr with an advective flow of  $v = 0.002$  are shown in Figure 7. A comparison between different advection speeds ( $v = 0.001c$ ,  $v = 0.002c$  and  $v = 0.003c$ ) is shown in Figure E4.

For further comparison of the gamma-ray morphology towards HESS J1825-137, the energy flux was extracted from rectangular regions taken along Galactic longitude centred on PSR J1826-1334 and are shown in Figure 8. An advective velocity of  $0.002c$  was chosen so that the peak in the modelled gamma-ray morphology in energy range  $E < 1 \text{ TeV}$  and  $1 \text{ TeV} < E < 10 \text{ TeV}$  corresponds to the HESS data (see the left-upper panel of Figure E4).

While an additional advective flow of  $0.002c$  lowered the gamma-ray SED towards HESS J1826-130 for energies less than 2 TeV, the emission still exceeds H.E.S.S. observations.

### 3.4.3 Model 3 - Isotropic Diffusion + Advection + Magnetic Field towards HESS J1826-130

As discussed in § 3.2.2, the turbulent molecular gas between HESS J1825-137 and HESS J1826-130 can act as a barrier for electrons escaping from the PWN. As clouds R1-R5 from Voisin et al. (2016) are positioned in an approximate semi-circle around PSR J1826-1256 (see Figure 3), Model 3 expanded on Model 2 ( $0.002c$ ) by including a shell of increased magnetic field strength,  $B_{1826}$ , centred on HESS J1826-130 with inner and outer radii  $0.17^\circ$  and  $0.33^\circ$  respectively. Model 3\* refers to Model 1 (40 kyr) with the shell of increased magnetic field strength with no advective component ( $v_A = 0$ ).



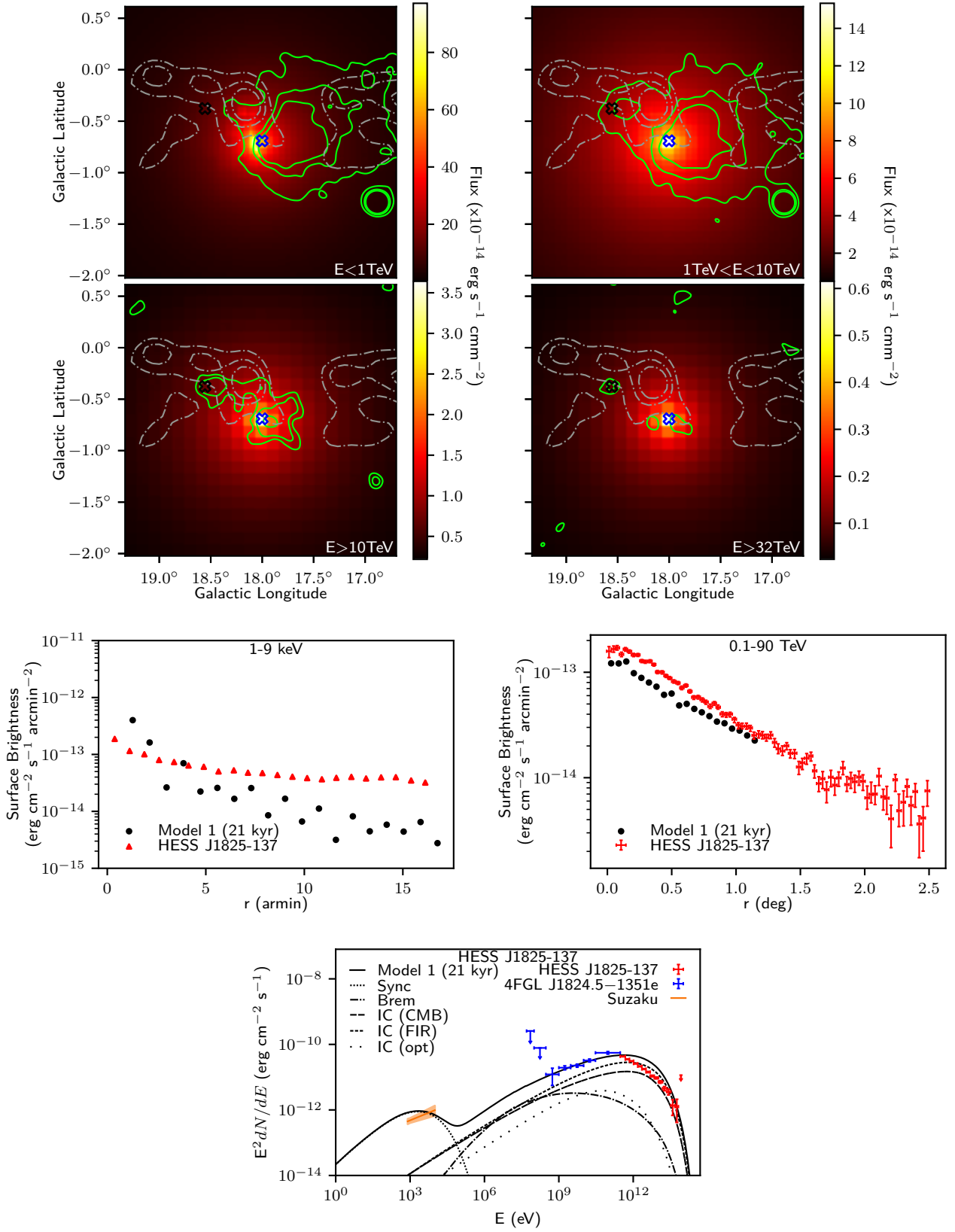


**Figure 4.** Model 1 (21 kyr), see Table 2 for model parameters. (*top & top-middle*) Modelled gamma-ray morphology towards HESS J1825-137 in different energy bands overlaid by green HESS significance contours (5, 10 and 15  $\sigma$  for  $E < 10 \text{ TeV}$  and 3, 5 and 10  $\sigma$  for  $E > 10 \text{ TeV}$ ) and grey 40, 50 and 60  $\sigma$  Nanten  $^{12}\text{CO}$  integrated intensity contours. The positions of PSR J1826-1334 and PSR J1826-1256 are indicated by the empty blue and black crosses respectively. (*bottom-middle*) 1 – 9 keV X-ray (*left*) and 1 – 91 TeV gamma-ray (*right*) surface brightness radial profiles in comparison to Suzaku (Uchiyama et al. 2009) and HESS observations (H.E.S.S. Collaboration et al. 2019) respectively. (*bottom*) SED towards HESS J1825-137 compared against the orange Suzaku X-ray spectral fit, blue 4FGL J1824.5-1351e flux points (Abdollahi et al. 2020) and red HESS J1825-137 flux points.

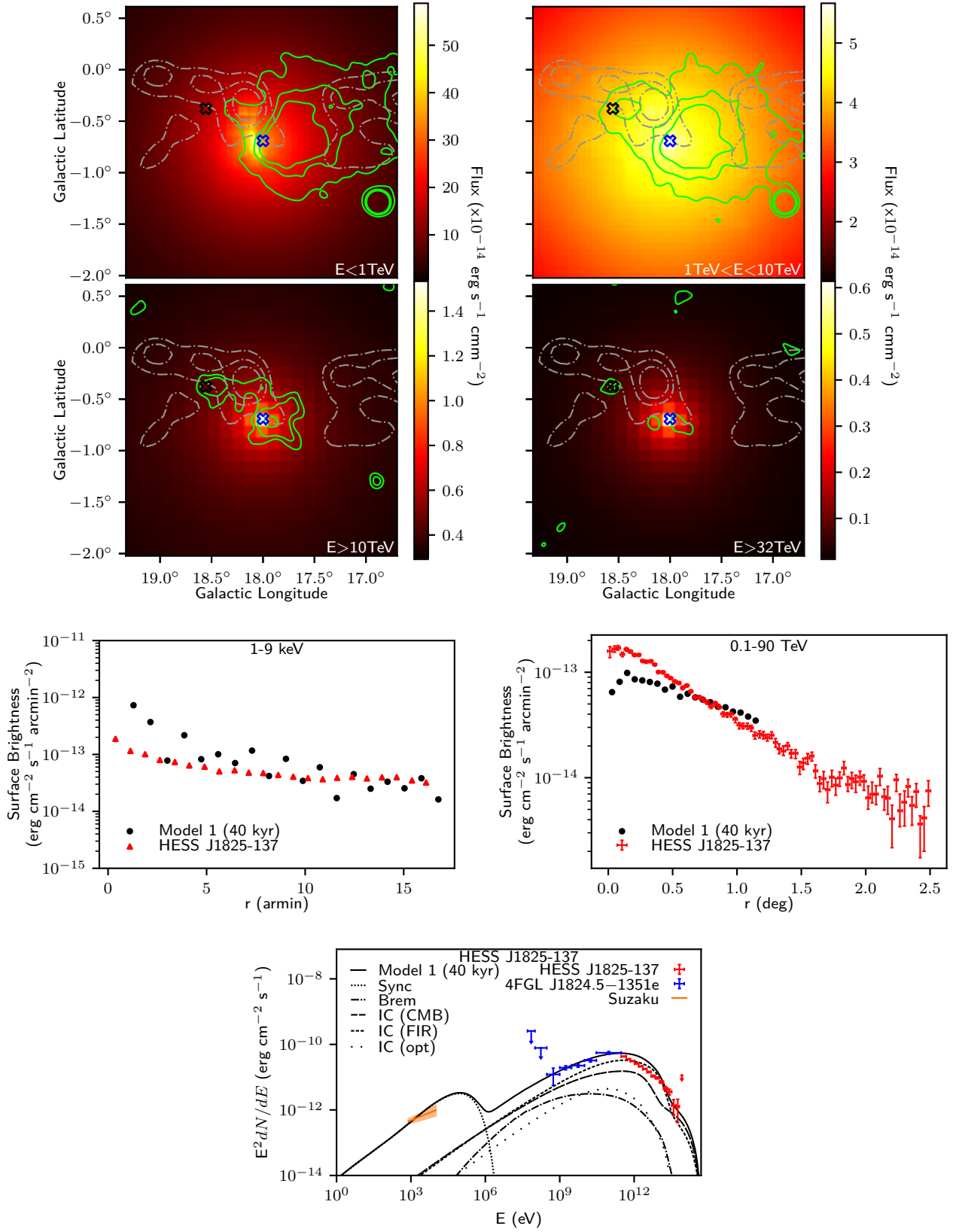


**Figure 5.** Model 1 (40 kyr), see Table 2 for model parameters. Same panel layout as in Figure 4.



**Table 2.** Modelled parameters that match the multi-wavelength SED and gamma-ray morphology towards HESS J1825-137. See section D for the 10% and 20% systematic variation of parameters.

Parameter	Model 1 (21 kyr)	Model 1 (40 kyr)	Model 2 (0.002c)	Model 3* (60 $\mu$ G)	Model 3 (60 $\mu$ G)
$\eta$	10.7	0.14	0.14	0.14	0.14
$\chi$	0.25	0.1	0.1	0.1	0.1
$\Gamma$	2.0	1.9	1.9	1.9	1.9
$E_c$ (TeV)	40	500	500	500	500
$B_0$ ( $\mu$ G)	70	450	450	450	450
$\beta$	-0.9	-0.7	-0.7	-0.7	-0.7
$n$	2	2	2	2	2
$V_A$	-	-	0.002c	-	0.002c
$B_{J1826}$ ( $\mu$ G)	-	-	-	60	60*

\* See § 3.5.3

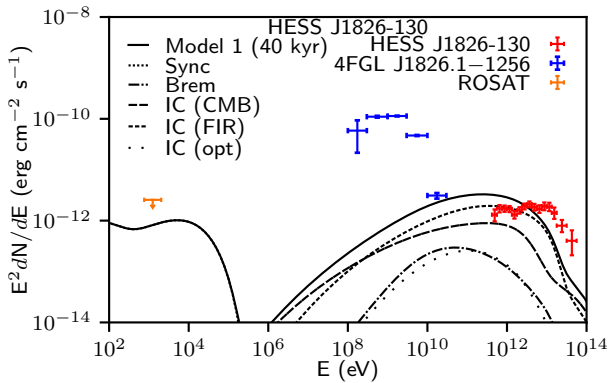


**Figure 6.** SED towards HESS J1826-130 from electrons accelerated by PSR 1826-1256 by Model 1 (40 kyr) against the observed flux of HESS J1826-130 (H.E.S.S. Collaboration et al. 2020) and 4FGL J1826.1-1256 (Abdollahi et al. 2020). The GeV and TeV gamma-ray flux points towards HESS J1826-130 are represented by blue and red respectively.

Figure 9 shows the SED, surface brightness radial profiles and the gamma-ray flux along Galactic longitude of HESS J1825-137 and HESS J1826-130 for Model 3 with magnetic field strengths of  $B = 20, 60$  and  $100 \mu\text{G}$ . A comparison between Model 1 (40 kyr), Model 3\* (60  $\mu\text{G}$ ) and Model 3 (60  $\mu\text{G}$ ) is shown in Figure 10 as well as the gamma-ray morphology for Model 3 (60  $\mu\text{G}$ ). All models have the same parameters as Model 1 (40 kyr) (see Table 2).

### 3.5 Discussion

#### 3.5.1 Model 1 - Isotropic Diffusion

The 21 kyr and 40 kyr models were unable to reproduce both the X-ray and gamma-ray surface brightness radial profiles. For example, the diffusion suppression coefficient,  $\chi$ , could be increased to compensate for the steep X-ray surface brightness radial profile for the 21 kyr model. Electrons would then escape the PWN at a higher rate and the gamma-ray surface brightness radial profile will flatten. This can be seen in the 40 kyr model, which assumes a lower value of  $\chi$  than the 21 kyr model. The shallow 40 kyr gamma-ray surface brightness radial profile indicates that lower energy electrons have started to accumulate near the pulsar, while high-energy electrons rapidly lose their energy through radiative cooling and do not escape far from the pulsar. This is demonstrated in the upper right panel in Figure 5 where the gamma-ray flux below 10 TeV is relatively constant over the grid while the flux above 10 TeV is constrained to the pulsar. This accumulation is not as apparent in

the 40 kyr X-ray surface brightness radial profile and the SED as the regions used in extracting X-ray spectra and surface brightness radial profile are smaller than the regions used for the gamma-ray analysis (see Figure 3 and top-middle right panel of Figure 4). The accumulation of lower-energy electrons is also reflected as a bump in the TeV gamma-ray SED. The bump occurs when synchrotron losses start to dominate at electron energies  $> 9$  TeV, resulting in inverse Compton radiation  $> 6$  TeV, and radiative energy losses are balanced by the electron injection luminosity (Manolakou et al. 2007; Hinton & Hofmann 2009). This bump is not present for a slightly younger age of 36 kyr (with the same parameters as Model 1 (40 kyr)) (see Figure E1), where the gamma-ray SED  $\gtrsim 10$  TeV at age 36 kyr matches Model 1 (40 kyr).

The 21 kyr model required a spin-down conversion factor of 10.7. To compensate, a braking index of 3 would inject a greater quantity of electrons at earlier times (see Equation 14). However, this results in an accumulation of electrons at lower energy, consequently increasing the gamma-ray flux for photons with energies  $< 1$  TeV (see Figure E2) and the modelled SED no longer reproduces observations. This suggests that the age of HESS J1825-137 lies between 21 kyr and 40 kyr. The 40 kyr magnetic field profile takes values of  $B_0 = 450 \mu\text{G}$  and  $\beta = -0.7$  (see Equation 15) in comparison to  $B_0 = 400 \mu\text{G}$  and  $\beta = -0.69$  used in (Van Etten & Romani 2011). Van Etten & Romani (2011) considered an evolving magnetic field  $B \propto \dot{E}(t)$  where the magnetic field takes larger values at earlier times. This could explain the larger  $B_0$  normalisation used in our modelling.

#### 3.5.2 Model 2 - Isotropic Diffusion + Advection

An advective component of  $0.002c$  towards lower Galactic longitudes was included into Model 1 (40 kyr).

The SED and X-ray surface brightness radial profile with an advective transportation component remains unchanged to Model 1 (40 kyr). Electrons rapidly escape the small ( $r = 0.05^\circ$ ) X-ray region, hence the subsequent X-ray SED and surface brightness radial profile depends more on the injected electron spectra rather than the method of transport. On the other hand, for both Model 1 (40 kyr) and Model 2 (0.002c), the majority of electrons remain within the large ( $0.7^\circ$ ) HESS region leaving the gamma-ray SED unchanged. However, the electrons in Model 2 have migrated further from the pulsar while remaining within the HESS region. Subsequently, the gamma-ray profile for Model 2 (0.002c) is flatter than Model 1 (40 kyr). Figure E3 shows the distance that electrons are transported before losing their energy to radiation. It can be seen that advection is the dominant particle transport method for electron energies less than 10 TeV, resulting in IC emission below 1 TeV.

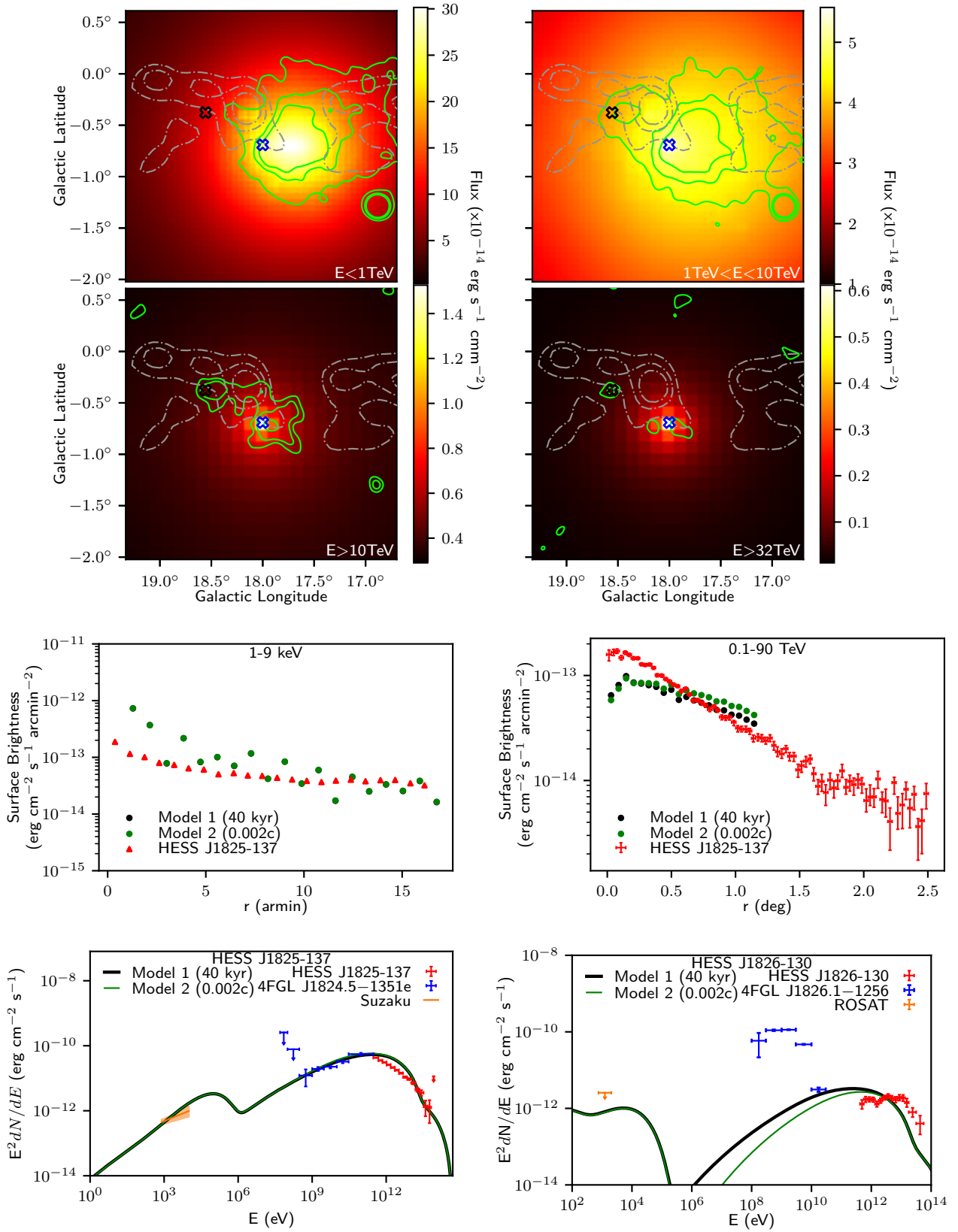


**Figure 7.** Model 2 (0.002c) vs Model 1 (40 kyr), see Table 2 for model parameters. (*top and top-middle*) panels show the gamma-ray morphology for Model 2 (0.002c). (*bottom-middle*) 1 – 9 keV X-ray (*left*) and 1 – 91 TeV gamma-ray (*right*) surface brightness radial profiles. (*bottom-left*) SED towards HESS J1825-137. (*bottom-right*) SED towards HESS J1826-130.

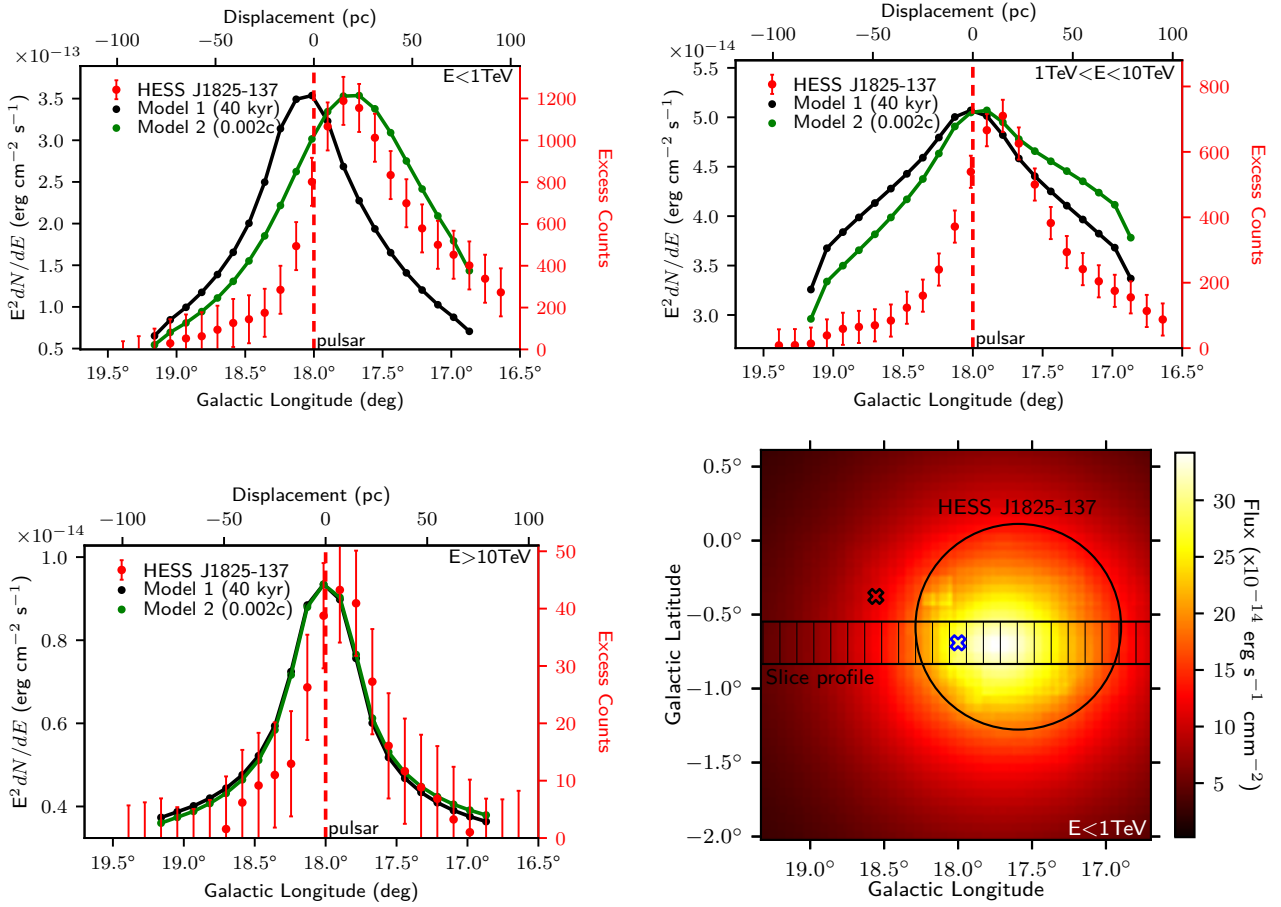


**Figure 8.** The energy flux along Galactic longitude for Model 1 (40 kyr, black) and Model 2 (0.002c, green) for energy bands  $E < 1$  TeV (top-left),  $1 < E < 10$  TeV (top-right) and  $E > 10$  TeV (bottom-left) vs HESS excess counts (H.E.S.S. Collaboration et al. 2019). (bottom-right) Model 2 (40 kyr) gamma-ray morphology for energies  $< 1$  TeV. The rectangular regions used to take the slice profile are indicated in black while the region used to extract the gamma-ray SED towards HESS J1825-137 is shown by the black circle. The positions of PSR J1826-1334 and PSR J1826-1256 are depicted by the blue and black empty crosses respectively. See Table 2 for model parameters.

Diffusion is dominant for electrons above 10 TeV. However, these high-energy electrons do not travel far from their birthplace before losing their energy to radiative cooling.

At all energies, the gamma-ray energy flux along Galactic longitude for Model 1 (40 kyr) appears symmetric around the pulsar position and shows no preferential direction of transportation. However, the HESS uncorrelated excess data indicates that electrons are preferential transported to lower Galactic longitudes. With the addition of an advective flow of 0.002c, the peak in the 40 kyr gamma-ray slices for photons less than 1 TeV is now offset from the pulsar and follows the shape of the uncorrelated excess. For the  $1 \text{ TeV} < E < 10 \text{ TeV}$  energy band, both Model 1 and Model 2 show a flatter slice profile compared to HESS observations. Electrons resulting from this emission appear to be contained near their birthplace before escaping into the nebula. Our model assumed that the diffusion index,  $\chi$ , lies within the Kraichnan regime ( $\delta = 0.3 - 0.6$ ) with the index being fixed at  $\delta = 0.5$ . The top-right panel of Figure 8 shows that the modelled gamma-ray slice morphology is broader than that observed by HESS, suggesting that electrons are constrained within the PWN. This suggests that the diffusion index inside the PWN may be somewhat less than the  $\delta = 0.5$  value we assumed, and perhaps to the lower bound for the Kraichnan regime.

By assuming that diffusion was isotropic in (as used in Equa-

tion 1), any preferential direction for particle transport was a result of ISM irregularities or advective flow. The highly asymmetric morphology towards HESS J1825-137 could be explained if diffusion is anisotropic with preferential diffusion towards lower Galactic longitudes. However, an anisotropic diffusion model can be approximated by an isotropic diffusion + advection model (i.e. Model 2).

### 3.5.3 Model 3 - Isotropic Diffusion + Advection + Magnetic Field towards HESS J1826-130

Here, a spherical shell of increased magnetic field strength around HESS J1826-130 was considered to replicate the turbulent gas towards cloud R1 from Voisin et al. (2016).

The bottom-right panel of Figure 8 shows that cloud R1 lies within the area used to determine the gamma-ray SED of HESS J1825-137. The ratio of synchrotron to inverse Compton flux is proportional to the magnetic field (Aharonian et al. 1997). Hence, as the magnetic field around HESS J1826-130 increases, electrons lose more energy through synchrotron losses and the inverse Compton flux decreases at equivalent gamma-ray energies. This can be seen in the SED for HESS J1825-137 in the bottom-middle right panel of Figure 9. This has the effect of improving the

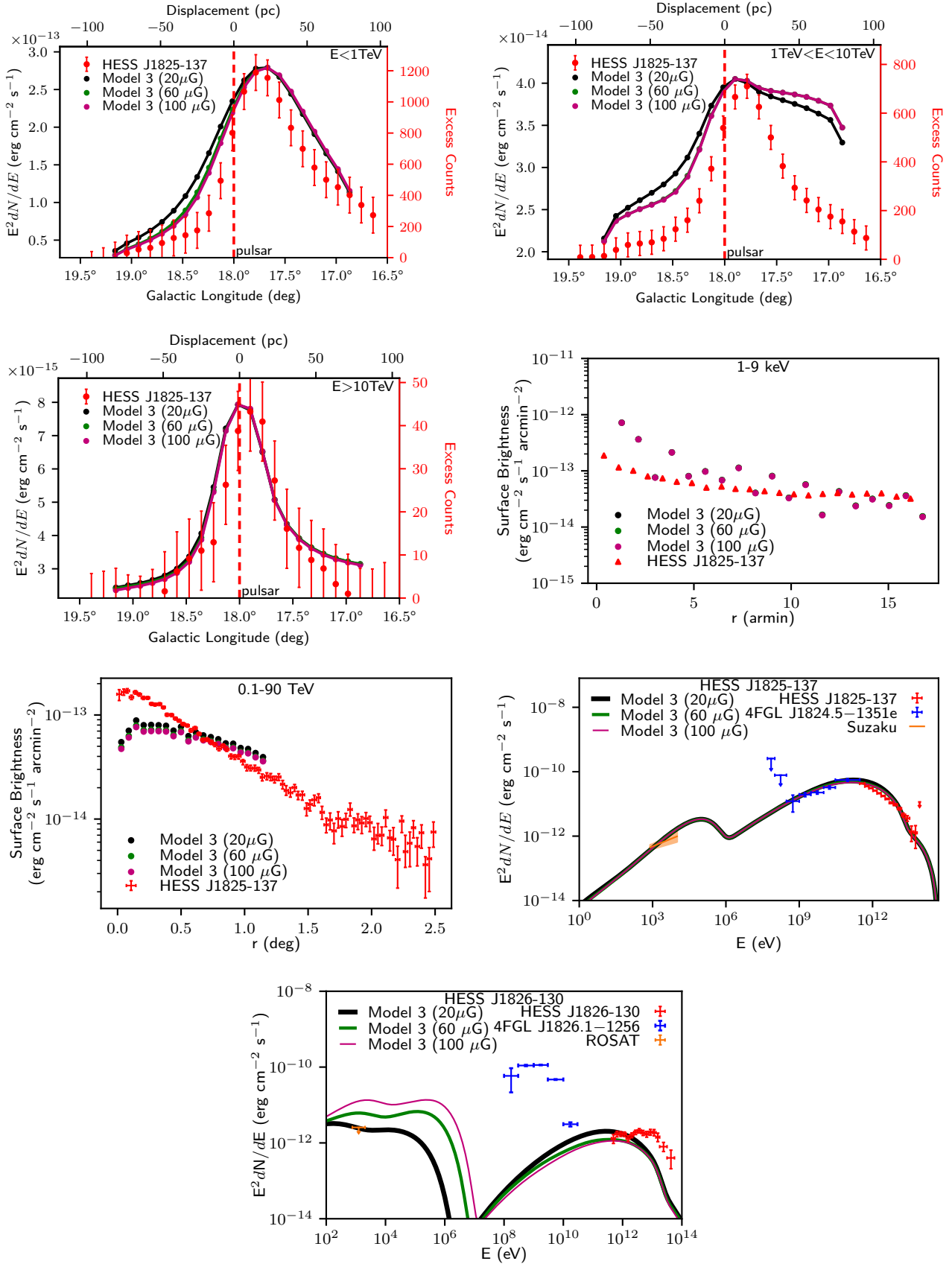


**Figure 9.** The energy flux along Galactic longitude profiles (top & top-middle left), surface brightness radial profiles (top-middle right & bottom-middle left) and SED towards HESS J1825-137 (bottom-middle right) and HESS J1826-130 (bottom) for Model 3 (20  $\mu\text{G}$ , black), (60  $\mu\text{G}$ , green) and (100  $\mu\text{G}$ , purple) around HESS J1826-130. See Table 2 for model parameters.

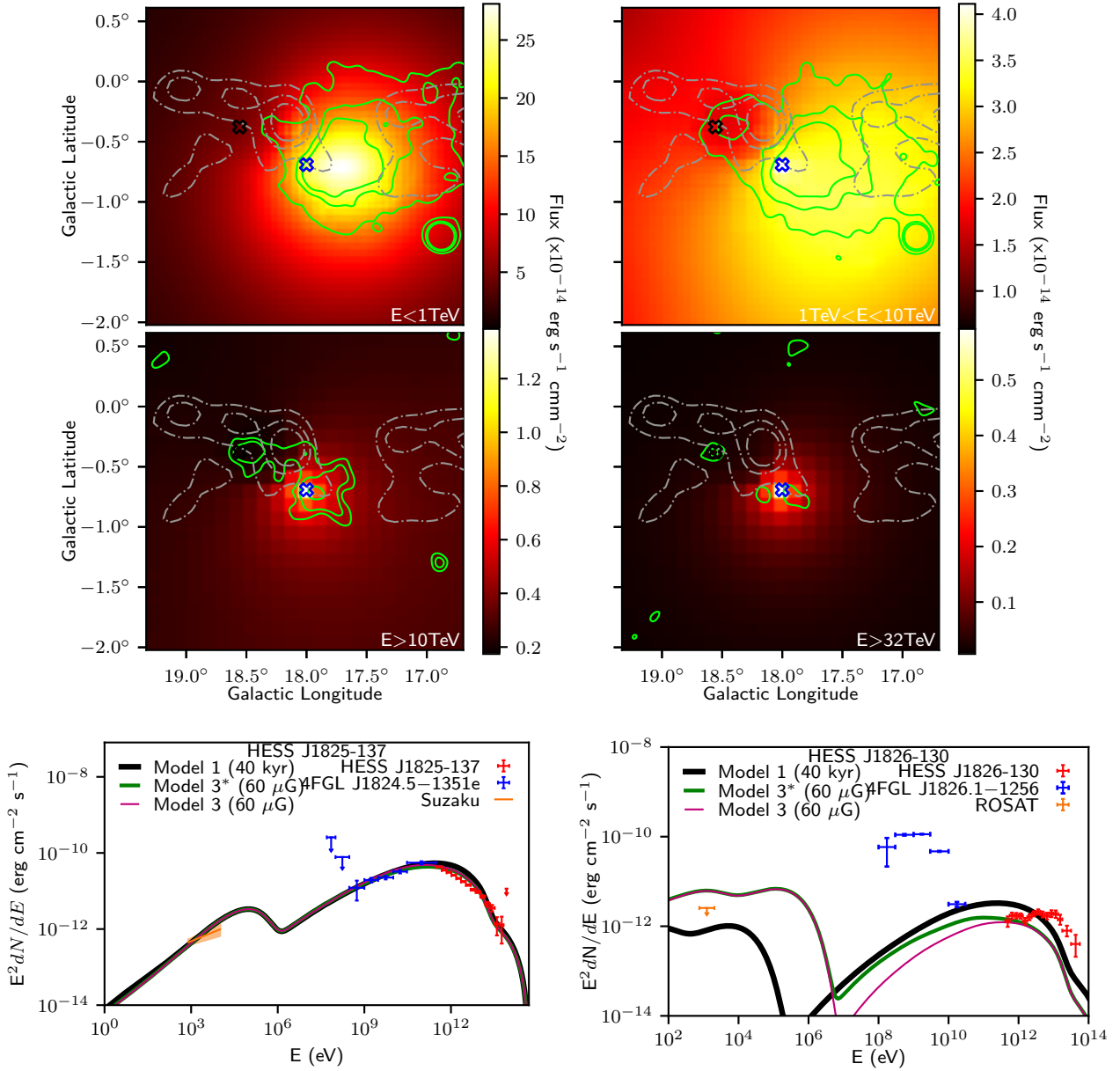


**Figure 10.** Comparison of the 40 kyr isotropic diffusion - Model 1 (40 kyr, black), Model 3\* (Model 1 + 60  $\mu$ G, green) and Model 3 (60  $\mu$ G, purple). The morphology plots towards HESS J1825-137 for Model 3 (60  $\mu$ G) are shown in the top and top-middle panels. See Table 2 for model parameters.

match (from 94% to 44% over-prediction) to HESS observations between 1 – 10 TeV compared to Model 1 (40 kyr) as shown in the bottom-middle-left panel of Figure 10.

The gamma-ray energy flux along Galactic longitude are shown in the top and top-middle panels of Figure 9. As the magnetic field around HESS J1826-130 increases, gamma-ray emission less than 1 < TeV and > 10 TeV remains unchanged at lower longitudes, with a decrease at higher longitudes. Between 1 TeV < E < 10 TeV, the gamma-ray slice profile drops off at a shallower rate compared to the HESS data at lower Galactic magnitudes. However the gamma-ray emission at higher longitudes, representing the area towards HESS J1826-130, increases proportionally with the magnetic field.

Additionally, the bottom-left panel of Figure 9 indicates that increasing the magnetic field strength around HESS J1826-130 lowers the contamination of HESS J1826-130 by the PWN associated

with HESS J1825-137 for energies < 2 TeV. Regions of high magnetic field strength experience a slower rate of diffusion (see Equation 6) and high synchrotron losses. Hence regions of high magnetic field tend to ‘block’ cosmic rays from passing through. The model implies that a minimum magnetic field strength of 60  $\mu$ G is required to successfully lower the contamination of HESS J1826-130 according to H.E.S.S. observations. The bottom-right panel of Figure 9 shows the multi-wavelength SED towards HESS J1826-130. An upper-limit to the X-ray emission towards HESS J1826-130 can be obtained using HEARSAC’s X-Ray background tool utilising ROSAT data (Sabot & Snowden 2019). The estimated synchrotron flux towards HESS J1826-130 combined with the ROSAT X-ray upper limit (obtained from the same region used to extract the SED of HESS J1826-130) implies a maximum magnetic field strength of  $\approx 20$   $\mu$ G around HESS J1826-130. This constraint violation sug-

gests that the model is not fully encapsulating the transport of particle between PSR 1826-1334 and HESS 1826-130.

### 3.6 Future Work

Presently, our model only considers isotropic diffusion and does not account for diffusion parallel and perpendicular to the magnetic field (Drury 1983; Lazarian et al. 2023). The magnetic fields of PWNe are believed to be toroidal in nature (Schmidt et al. 1979; Kothes et al. 2006), hence diffusion is expected to be suppressed perpendicular to the magnetic axis of the pulsar. Additionally, the recent detection of TeV halos (Abeysekara et al. 2017) implies that the region surrounding the PWN experiences a higher diffusion suppression compared to the average Galactic diffusion coefficient (Schroer et al. 2023). While current models of particle transport suggest that advection dominates particle transport within the PWN and diffusion dominates at the edges, this could be described by two different regions of diffusion suppression. Model 2 and 3 in this study considered spatially-independent advection towards lower Galactic longitudes to explain the asymmetric TeV gamma-ray morphology towards HESS J1825-137. As a result, losses due to adiabatic expansion were neglected. Future modelling of PWNe with in particular HESS J1825-137 could investigate the effects of spatially-dependent anisotropic diffusion and an azimuthal and surface brightness dependent advective velocity on the gamma-ray morphology and SED. This can then be applied to model the formation of the TeV halo around HESS J1825-137 (Principe et al. 2020).

Our model assumed a time-independent magnetic field with decreasing strength from the distance to the pulsar (see § 3.2.1). However, the average magnetic field of PWNe are expected to decrease over time from the conservation of magnetic energy density (e.g. (Tanaka & Takahara 2010)) and the normalisation,  $B_0$ , obtained from the modelling (see Table 2) can be considered as the time-averaged normalisation. Any future predictions of the formation of the TeV halo around HESS J1825-137 must consider time-dependency on the magnetic field.

The implementation of a time-dependent source position will not affect the gamma-ray morphology  $\gtrsim 13$  TeV around PSR J1826-1334 due to high synchrotron losses. However, lower energy photons will appear to originate at a position offset to the current position of the pulsar as seen in Principe et al. (2020). This does not explain the extended TeV gamma-ray morphology towards lower Galactic longitudes as discussed in section 3, but could affect the modelled formation of the TeV halo. Future work could investigate the affects of an evolving source position on the gamma-ray surface brightness radial profile and morphology towards PWNe and other sources. For example, the application of our model to SNRs would require cosmic rays to be injected by an expanding shell to model diffusive shock acceleration by the expanding SNR.

The model presented in this study is not limited to HESS J1825-137 and can be used to model the transport of cosmic rays (electrons and protons) from other PWN and cosmic ray sources.

## 4 SUMMARY

By modelling the transport of electrons across a 3D Cartesian grid of varying ISM density and magnetic field, we are able to reproduce the multi-wavelength emission and morphology towards HESS J1825-137. Three different models were considered. Model 1 assumed a simple case of isotropic diffusion and radiative losses for

the characteristic age of 21 kyr and an older age of 40 kyr suggested by Van Etten & Romani (2011). Model 2 included an additional advective component to Model 1 (40 kyr) and Model 3 introduced turbulent ISM towards HESS J1826-130 to Model 2.

The best fit 21 kyr and 40 kyr Model 1 consisted of a pulsar injecting electrons into the surrounding medium with a spin-down conversion factor of 10.7 and 0.14% respectively, indicating that the true age of the system is older than the characteristic age of PSR J1826-1334. While able to reproduce the multi-wavelength SED, neither model was able to sufficiently reproduce the gamma-ray morphological profile described in H.E.S.S. Collaboration et al. (2019) for photons with energies  $1 \text{ TeV} < E < 10 \text{ TeV}$ . However, the morphological profile could be matched for gamma-rays with energies  $< 1 \text{ TeV}$  (with an offset of  $\sim 0.3^\circ$  towards higher Galactic longitudes compared to the HESS data) and energies  $> 10 \text{ TeV}$ .

Applying an advective bulk flow (with velocity  $v = 0.002c$ ) of electrons towards lower Galactic longitudes did not alter the photon SED predicted by Model 1. By taking the energy flux along Galactic longitude, we were able to compare in detail the gamma-ray morphology towards HESS J1825-137. Model 2 ( $0.002c$ ) was able to reproduce the energy flux for photons  $< 1 \text{ TeV}$  and  $> 10 \text{ TeV}$ , however photons with energies  $1 < E < 10 \text{ TeV}$  experience a shallower drop-off compared to the uncorrelated HESS excess slices as revealed by H.E.S.S. Collaboration et al. (2019). This suggests that the parent electrons are constrained within the PWN before escaping into the interstellar medium to form a TeV halo.

As the gamma-ray emission associated with PSR 1826-1334 cannot exceed the observed emission towards HESS J1826-130, HESS J1826-130 can be used to constrain the model. Model 1 and Model 2 were found to over-predict the SED of HESS J1826-130 for photons  $< 1.5 \text{ TeV}$ . By placing a shell of increased magnetic field strength of at least  $60 \mu\text{G}$  around HESS J1826-130, representing the turbulent gas between the two HESS sources (Voisin et al. 2016), the contamination was successfully lowered below the levels closer to those estimated by HESS. By combining the modelled synchrotron flux with the ROSAT X-ray upper limit towards HESS J1826-130, we were able to constrain the magnetic field shell to have maximum strength of  $20 \mu\text{G}$ . This constraint violation suggests that further modelling of the turbulent gas is needed to fully disentangle the particle transport towards HESS J1825-137.

## ACKNOWLEDGEMENTS

T. Collins acknowledges support through the provision of Australian Government Research Training Program Scholarship.

The Nanten project is based on a mutual agreement between Nagoya University and the Carnegie Institution of Washington (CIW). We greatly appreciate the hospitality of all the staff members of the Las Campanas Observatory of CIW. We are thankful to many Japanese public donors and companies who contributed to the realization of the project.

This research has made use of the NASA's Astrophysics Data System and the SIMBAD data base, operated at CDS, Strasbourg, France.

## DATA AVAILABILITY

No new data were generated or analysed in support of this research.



## REFERENCES

- Abdollahi S., et al., 2020, *ApJS*, 247, 33
- Abeysekara A. U., et al., 2017, *Science*, 358, 911
- Abeysekara A. U., et al., 2020, *Phys. Rev. Lett.*, 124, 021102
- Aharonian F. A., Atoyan A. M., 1996, *A&A*, 309, 917
- Aharonian F. A., Atoyan A. M., Kifune T., 1997, *MNRAS*, 291, 162
- Aharonian F., et al., 2005, *Science*, 307, 1938
- Araya M., Mitchell A. M. W., Parsons R. D., 2019, *MNRAS*, 485, 1001
- Atoyan A. M., Aharonian F. A., Völk H. J., 1995, *Phys. Rev. D*, 52, 3265
- Benbow W., 2005, in Aharonian F. A., Völk H. J., Horns D., eds, *American Institute of Physics Conference Series Vol. 745, High Energy Gamma-Ray Astronomy*. pp 611–616, doi:10.1063/1.1878471
- Berezinskii V. S., Bulanov S. V., Dogiel V. A., Ptuskin V. S., 1990, *Astrophysics of cosmic rays*. John Wiley & Sons, Inc.
- Blumenthal G. R., Gould R. J., 1970, *Reviews of Modern Physics*, 42, 237
- Brand J., Blitz L., 1993, *A&A*, 275, 67
- Brogan C. L., Gelfand J. D., Gaensler B. M., Kassim N. E., Lazio T. J. W., 2006, *ApJ*, 639, L25
- Cao Z., et al., 2021, *Nature*, 594, 33
- Castor J., McCray R., Weaver R., 1975, *ApJ*, 200, L107
- Cesarsky C. J., Volk H. J., 1978, *A&A*, 70, 367
- Collins T., Rowell G., Mitchell A. M. W., Voisin F., Fukui Y., Sano H., Alsulami R., Einecke S., 2021, *MNRAS*,
- Cordes J. M., Lazio T. J. W., 2002, *arXiv e-prints*, pp astro-ph/0207156
- Crutcher R. M., Wandelt B., Heiles C., Falgarone E., Troland T. H., 2010, *ApJ*, 725, 466
- Drury L. O., 1983, *Reports on Progress in Physics*, 46, 973
- Gabici S., Aharonian F. A., Blasi P., 2007, *Ap&SS*, 309, 365
- Gabici S., Casanova S., Aharonian F. A., Rowell G., 2010, in Boissier S., Heydari-Malayeri M., Samadi R., Valls-Gabaud D., eds, *SF2A-2010: Proceedings of the Annual meeting of the French Society of Astronomy and Astrophysics*. p. 313 (arXiv:1009.5291)
- Gaensler B. M., Slane P. O., 2006, *ARA&A*, 44, 17
- Giacinti G., Mitchell A. M. W., López-Coto R., Joshi V., Parsons R. D., Hinton J. A., 2020, *A&A*, 636, A113
- Giuliani A., et al., 2010, *A&A*, 516, L11
- H.E.S.S. Collaboration et al., 2018a, *A&A*, 612, A1
- H.E.S.S. Collaboration et al., 2018b, *A&A*, 612, A2
- H.E.S.S. Collaboration et al., 2019, *A&A*, 621, A116
- H.E.S.S. Collaboration et al., 2020, *A&A*, 644, A112
- Haensel P., Potekhin A. Y., Yakovlev D. G., 2007, *Neutron Stars 1: Equation of State and Structure*. Springer, New York
- Hinton J. A., Hofmann W., 2009, *ARA&A*, 47, 523
- Isaacson E., 1966, *Analysis of numerical methods*. Wiley, New York
- Kothes R., Reich W., Uyaniker B., 2006, *ApJ*, 638, 225
- Lazarian A., Xu S., Hu Y., 2023, *Frontiers in Astronomy and Space Sciences*, 10, 1154760
- Lemoine M., Pelletier G., 2010, *MNRAS*, 402, 321
- Li H., Chen Y., 2010, *MNRAS*, 409, L35
- Manchester R. N., Hobbs G. B., Teoh A., Hobbs M., 2005, *AJ*, 129, 1993
- Manolakou K., Horns D., Kirk J. G., 2007, *A&A*, 474, 689
- Mizuno A., Fukui Y., 2004, in Clemens D., Shah R., Brainerd T., eds, *Astronomical Society of the Pacific Conference Series Vol. 317, Milky Way Surveys: The Structure and Evolution of our Galaxy*. p. 59
- Odegard N., 1986, *AJ*, 92, 1372
- Popescu C. C., Yang R., Tuffs R. J., Natale G., Rushton M., Aharonian F., 2017, *MNRAS*, 470, 2539
- Porth O., Vorster M. J., Lyutikov M., Engelbrecht N. E., 2016, *MNRAS*, 460, 4135
- Principe G., Mitchell A. M. W., Caroff S., Hinton J. A., Parsons R. D., Funk S., 2020, *A&A*, 640, A76
- Prosekin A. Y., Kelner S. R., Aharonian F. A., 2015, *Phys. Rev. D*, 92, 083003
- Protheroe R. J., Ott J., Ekers R. D., Jones D. I., Crocker R. M., 2008, *MNRAS*, 390, 683
- Sabol E. J., Snowden S. L., 2019, *srbg: ROSAT X-Ray Background Tool*, *Astrophysics Source Code Library*, record ascl:1904.001

(ascl:1904.001)

- Sano H., et al., 2017, *ApJ*, 843, 61
- Schmidt G. D., Angel J. R. P., Beaver E. A., 1979, *ApJ*, 227, 106
- Schroer B., Evoli C., Blasi P., 2023, *Phys. Rev. D*, 107, 123020
- Sironi L., Keshet U., Lemoine M., 2015, *Space Sci. Rev.*, 191, 519
- Skilling J., 1975, *MNRAS*, 172, 557
- Strong A. W., Moskalenko I. V., Reimer O., Digel S., Diehl R., 2004, *A&A*, 422, L47
- Strong A. W., Moskalenko I. V., Ptuskin V. S., 2007, *Annual Review of Nuclear and Particle Science*, 57, 285
- Stupar M., Parker Q. A., Filipović M. D., 2008, *MNRAS*, 390, 1037
- Tanaka S. J., Takahara F., 2010, *ApJ*, 715, 1248
- Taylor J. H., Cordes J. M., 1993, *ApJ*, 411, 674
- Uchiyama H., Matsumoto H., Tsuru T. G., Koyama K., Bamba A., 2009, *PASJ*, 61, S189
- Van Etten A., Romani R. W., 2011, *ApJ*, 742, 62
- Voisin F., Rowell G., Burton M. G., Walsh A., Fukui Y., Aharonian F., 2016, *MNRAS*, 458, 2813
- Weaver R., McCray R., Castor J., Shapiro P., Moore R., 1977, *ApJ*, 218, 377
- de Jager O. C., Djannati-Ataï A., 2009, in Becker W., ed., *Astrophysics and Space Science Library Vol. 357, Astrophysics and Space Science Library*. p. 451 (arXiv:0803.0116), doi:10.1007/978-3-540-76965-1\_17

## APPENDIX A: NON-THERMAL EMISSION

This section will provide an overview of leptonic interactions and the subsequent photon emission via Synchrotron, Bremsstrahlung and inverse Compton Processes.

Synchrotron interactions occur when an electron interacts with background magnetic fields. The resulting SED emission from a single electron with Lorentz factor  $\gamma$  with pitch angle  $\alpha$  to the magnetic field  $B$  is given by:

$$P(\nu) = \frac{\sqrt{3}e^3 B}{mc^2} \frac{\nu}{\nu_c} \int_{\frac{\nu}{\nu_c}}^{\infty} K_{\frac{5}{3}}(x) dx, \quad (\text{A1})$$

where  $e$  and  $m$  are the charge and mass of an electron respectively,  $K_{\frac{5}{3}}$  is the modified Bessel Function,  $\nu$  is the frequency of the gamma ray and  $\nu_c$  is the critical frequency of the emission:

$$\nu_c = \gamma^2 \frac{3eB \sin \alpha}{4\pi mc}. \quad (\text{A2})$$

The inverse Compton gamma-ray SED from an electron with energy  $E_e$  scattering off a target photon with energy in range  $(\epsilon + d\epsilon)$  and number density  $n(\epsilon)$  can be found using:

$$\frac{dN}{dE_\gamma} = \frac{3\sigma_T mc^3}{4\gamma} \int_{E_\gamma/4\gamma^2}^{E_\gamma} \frac{n(\epsilon) d\epsilon}{\epsilon} f(q, \Gamma) \quad (\text{A3a})$$

$$f(q, \Gamma) = 2q \ln q + (1 + 2q)(1 - q) + \frac{1}{2} \frac{(\Gamma q)^2}{1 + \Gamma q} (1 - q) \quad (\text{A3b})$$

$$q = \frac{E_\gamma}{\Gamma(E_e - E_\gamma)}, \quad \Gamma = \frac{4\epsilon\gamma}{mc^2} \quad (\text{A3c})$$

where  $\sigma_T = (3/8\pi)r_0^2$  is the Thompson cross section,  $r_0$  is the classical electron radius and  $F_{\text{KN}}$  takes account the full Klein-Nishina cross section for Inverse Compton scattering (Manolakou et al. 2007):

$$F_{\text{KN}} = \frac{1}{u_0} \int_0^\infty \mathcal{F}(\gamma, \epsilon) u_\epsilon d\epsilon, \quad \mathcal{F}(\gamma, \epsilon) = (1 + 4\gamma\epsilon)^{-\frac{3}{2}}. \quad (\text{A4})$$

For a Planckian distribution of photon energies,  $F_{\text{KN}}$  can be approximated by:

$$F_{\text{KN}} = (1 + 4\gamma\epsilon_{\text{eff}})^{-3/2}, \quad \epsilon_{\text{eff}} = \frac{2.8kT}{m_e c^2}. \quad (\text{A5})$$

Finally, the gamma-ray SED from Bremsstrahlung interactions is given by:

$$\frac{dN}{dE_\gamma} = nc \int d\sigma(E_e, E_\gamma, Z) dE_e, \quad (\text{A6})$$

where  $Z$  is the atomic number of the target material and  $d\sigma$  is the bremsstrahlung differential cross section as defined in Blumenthal & Gould (1970).

The coefficients for leptonic losses in Equation 4 are:

- $b_s = 1.292 \times 10^{-15} (B/10^3 \mu\text{G})^2 \text{ s}^{-1}$  is the synchrotron loss coefficient
- $b_c = 1.491 \times 10^{-14} (n_H/1 \text{ cm}^{-3})$  is the Coulomb loss coefficient
- $b_b = 1.37 \times 10^{-16} (n_H/1 \text{ cm}^{-3}) \text{ s}^{-1}$  is the Bremsstrahlung loss coefficient
- $b_{\text{IC}} = 5.204 \times 10^{-20} (u_0/\text{eV}) \text{ s}^{-1}$  is the IC loss coefficient with the energy density of photons given by  $u_0$
- $n_H$  is the density of the ambient hydrogen gas

The diffusion radius for electrons (Atoyan et al. 1995):

$$R_{\text{diff}} = \sqrt{\frac{4D(\gamma)}{b_s \gamma (1 - \delta)} \left[ 1 - (1 - \gamma b_s t)^{1 - \delta} \right]}. \quad (\text{A7})$$

## APPENDIX B: MAGNETIC FIELD DUE TO TURBULENT ISM GAS

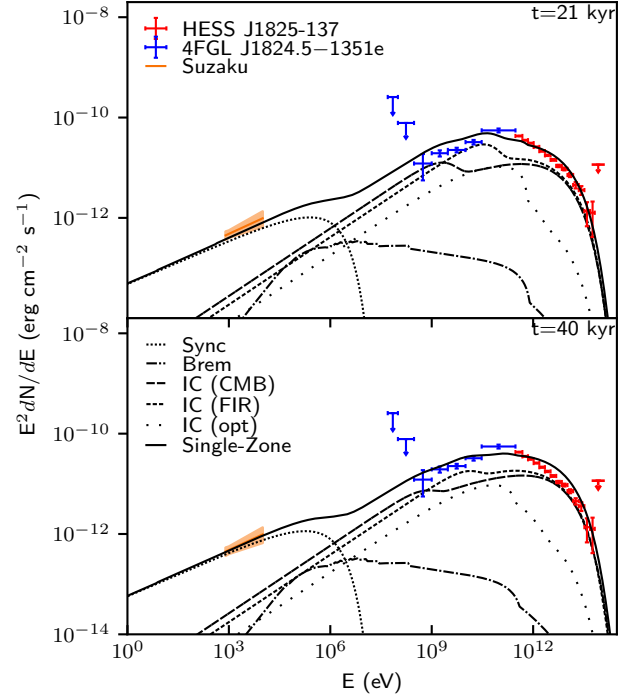
The magnetic field due to the ISM gas with number density  $n$  is given through Crutcher's relation (Crutcher et al. 2010):

$$B_{\text{gas}}(n) = \begin{cases} B_{0,\text{gas}}, & n < 300 \text{ cm}^{-3} \\ B_{0,\text{gas}} (n/300 \text{ cm}^{-3})^\alpha, & n > 300 \text{ cm}^{-3} \end{cases}, \quad (\text{B1})$$

where  $B_{0,\text{gas}} = 10 \mu\text{G}$  and  $\alpha = 0.65$ .

## APPENDIX C: SINGLE-ZONE MODELLING

Here we considered a 'single-zone' model, where electrons are injected into a spherical region of constant number density and magnetic field (Sano et al. 2017; Collins et al. 2021). The final electron number density is calculated by solving Eq. C7 from Collins et al. (2021) over the age of the system where electrons escape the region at a rate dependent on diffusion. The subsequent multi-wavelength SED from this region is then calculated. While unable to encapsulate the complexity towards HESS J1825-137, a general insight of the system was gained before more detailed modelling of the morphology and time evolution.



Parameter	$t = 21 \text{ kyr}$		$t = 40 \text{ kyr}$	
	HESS	Suzaku	HESS	Suzaku
$\dot{E}$ (erg s $^{-1}$ )	$2 \times 10^{38}$	$8 \times 10^{35}$	$1 \times 10^{38}$	$4 \times 10^{35}$
$r$ (°)	0.70	0.025	0.70	0.025
$n$ (cm $^{-3}$ )	0.5	0.5	0.5	0.5
$B$ (μG)	5	40	5	40
$\chi$	0.25	0.25	0.1	0.1
$\Gamma$	2.1	1.9	2.1	1.9
$E_c$ (TeV)	40	1000	50	1000

**Figure C1.** SED for leptonic interactions towards HESS J1825-137 using single-zone modelling. The X-ray and gamma-ray spectra are fitted separately due to the different coverage areas of HESS and Suzaku. The orange line shows the Suzaku match of X-rays between 1 – 9 keV towards the pulsar associated with HESS J1825-137 (Uchiyama et al. 2009). Blue data points represent the spectrum from the *Fermi*-LAT 4FGL source catalogue towards HESS J1825-137 while the red data shows the H.E.S.S. energy flux towards HESS J1825-137 (H.E.S.S. Collaboration et al. 2019). The top and bottom panels are at ages 21 kyr and 40 kyr respectively. The corresponding model parameters is shown in the table.

## C1 Method

The multi-zone Suzaku X-ray and HESS gamma-ray SED was extracted using two different areas with radii  $r_{\text{X-ray}}$  and  $r_{\text{gamma}}$  (see Figure 3). Consequently, the X-ray and gamma-ray emission must be modelled separately utilising single zone modelling.

Supernovae tend to leave a bubble of low-density gas in the interstellar medium. Within the extent of the PWN, the density of both regions was set to  $0.5 \text{ cm}^{-3}$ . Electrons were injected into the ISM at a constant rate  $\dot{E}$  and followed a power-law spectrum with an exponential cutoff:  $\frac{dN}{dE} \propto E^{-\Gamma} \cdot \exp(-E/E_c)$ , where  $\Gamma$  is the spectral index and  $E_c$  is the cutoff energy. Two different ages were modelled, 21 kyr based on the characteristic age of the pulsar and 40 kyr based on modelling conducted by (Van Etten & Romani 2011).

The HESS region adopted a uniform magnetic field of  $5 \mu\text{G}$  as suggested by Principe et al. (2020) from comparing the estimated synchrotron emission to the Suzaku X-ray emission. Subsequently, it was assumed that the smaller X-ray region has a higher magnetic

field strength than the HESS region due to the proximity of the pulsar and was left as a free parameter.

The fits to the SED towards HESS J1825-137 as well as the modelled parameters can be seen in Figure C1.

## C2 Discussion

Figure C1 shows the modelled SED with corresponding parameters to the gamma and X-ray spectra towards HESS J1825-137. The majority of gamma rays in this model are predicted to come from inverse Compton interactions from the infrared and CMB photon fields. An electron injection luminosity of  $2 \times 10^{38}$  and  $1 \times 10^{38} \text{ erg s}^{-1}$  is needed to match the gamma-ray spectra at ages 21 and 40 kyr respectively. This is a factor ten times greater than the spin-down power of PSR 1826-1334 ( $\dot{E} = 2.8 \times 10^{36} \text{ erg s}^{-1}$ ). The single-zone model assumes a time-independent injection luminosity, whereas the spin-down power of the pulsar decreases over time. The spin-down power of PSR 1826-1334 could have been as high as  $10^{39} \text{ erg s}^{-1}$  at a pulsar age of 1 kyr (see subsection 3.1). Therefore the modeled injection luminosities represents the average electron injection luminosity over the age of the pulsar.

The X-ray emission towards PSR 1826-1334 can be predicted with an injection luminosity of  $8 \times 10^{35} \text{ erg s}^{-1}$  and  $4 \times 10^{35} \text{ erg s}^{-1}$  for the 21 and 40 kyr model respectively. The single-zone model can reasonably predict both the X-ray and gamma-ray SED, yet the X-ray and gamma-ray photon models require different injection spectra for both ages of the system. The single-zone model assumes constant density and magnetic field strength across the region of interest. However, the magnetic field structures towards PWNe have been suggested to be toroidal in nature but the viewing angle results in magnetic fields appearing radially dependent or tangled (Koties et al. 2006). If the dense clouds towards HESS J1826-130, as seen in Figure 3, lie at the same distance as the pulsar, diffusion will be suppressed towards this region with electrons losing their energy to bremsstrahlung losses. As previously mentioned, the spin-down power of the pulsar decreases over time which has an effect on the injection luminosity of electrons in the ISM. While the single-zone model is able to predict the X-ray and gamma-ray SED towards HESS J1825-137, it is unable to encapsulate the complexity of the PWN.

## APPENDIX D: SYSTEMATIC VARIATION OF MULTIZONE PARAMETERS

Figure D1 and Figure D2 shows the 10% and 20% systematic variation of the free parameters  $\beta$ ,  $B_0$ ,  $\chi$ ,  $\Gamma$ ,  $E_c$  and  $\eta$  for the 21 kyr and 40 kyr models. These figures show that the spectral index of injection electrons,  $\Gamma$ , has the largest systematic variation, where the X-ray SED and surface brightness radial profiles show more sensitivity than the gamma-ray emission. This is a result of the smaller region used to extract the X-ray and SED (see Figure 3 and Figure 4).

The modelled X-ray surface brightness radial profiles for the 21 and 40 kyr models are steeper than observations, indicating that the model over-predicts the synchrotron emission closer to PSR 1826-1334. This may be corrected by decreasing the rate at which the magnetic field drops off with distance from the pulsar ( $\beta$ ), allowing electrons to escape the PWN at a faster rate. The outer edges of the PWN experiences greater synchrotron losses at the cost of TeV gamma-ray emission from IC interactions, flattening out the gamma-ray surface brightness radial profile. This is demonstrated

in the 10 and 20% variation of  $\beta$  shown in the top row of Figure D1 and Figure D2. Alternatively, decreasing the overall magnetic field strength,  $B_0$ , decreases synchrotron losses towards HESS J1825-137 at the cost of increasing the gamma-ray to X-ray flux ratio. With flux being dependent on the observational area, any changes to the gamma-ray and X-ray ratio will be more prominent in the X-ray SED as shown in Figure D1 and Figure D2.

To better fit the X-ray surface brightness radial profile, the diffusion suppression coefficient,  $\chi$ , towards HESS J1825-137 could be increased to allow electrons to escape further from the pulsar before losing their energy to synchrotron radiation. High-energy electrons rapidly lose their energy to radiative losses and remain close to the pulsar, resulting in a shallower gamma-ray surface brightness radial profile as shown in Figure D1 and Figure D2. As the region used to extract the X-ray data is small ( $< 2pc$ ) compared to the HESS region ( $\approx 49 pc$ ), electrons quickly escape the X-ray region while remaining in the HESS region. Thus the X-ray SED far more sensitive to the value of  $\chi$  than the gamma-ray SED.

Both the surface brightness radial profiles and SED are very sensitive to the injected electron spectral index,  $\Gamma$ , as seen in Figure D1 and Figure D2. If  $\beta$ ,  $B_0$  or  $\chi$  was altered to fit the observed Suzaku X-ray surface brightness radial profile, the predicted SED from the model will no longer fit to the data. In turn, the spectral index can be modified to refit the modelled SED. Consequently, the X-ray surface brightness radial profile will no longer match the Suzaku observations.

The cutoff energies for the 21 kyr and 40 kyr models are 45 TeV and 500 TeV respectively. As the cutoff energy for an exponential cutoff power-law increases, the energy spectra starts to follow a power-law. Hence, the systematic variation of  $E_c$  is less apparent for 40 kyr than 21 kyr as seen in the fourth row of Figure D1 and Figure D2 respectively.

## APPENDIX E: ADDITIONAL FIGURES

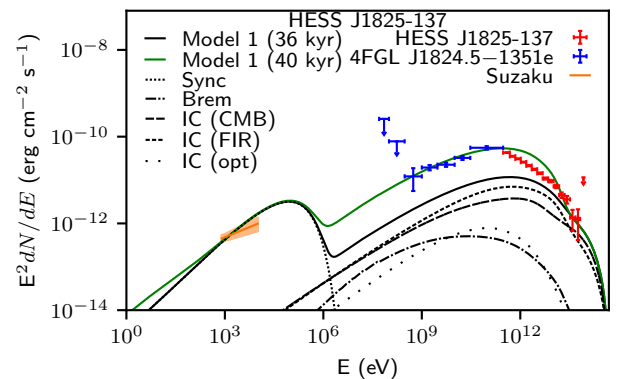
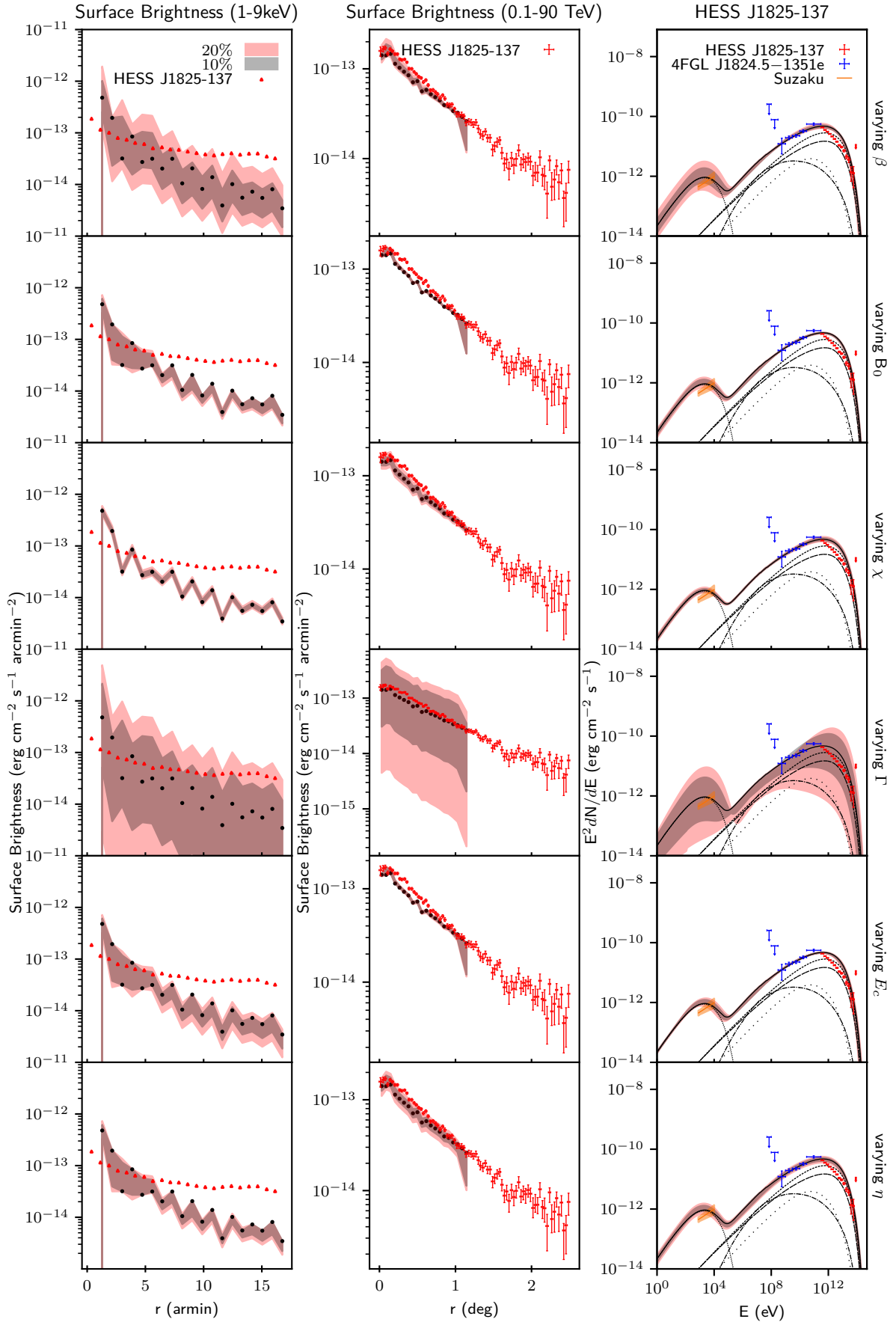
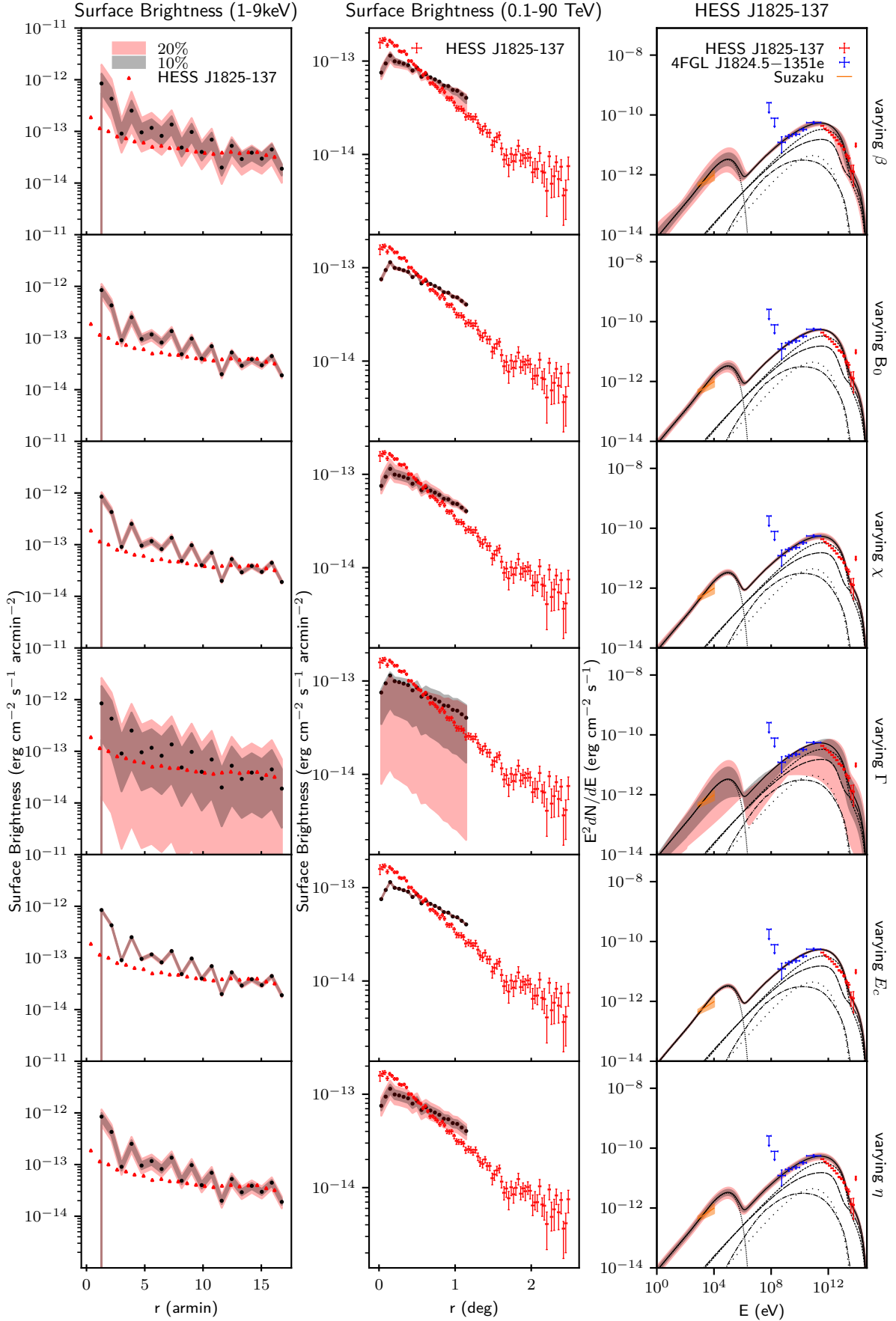


Figure E1: SED towards HESS J1825-137 for Model 1 (36 kyr, green) shown vs Model 1 (40 kyr). A ‘bump’ is present in the SED above 10 TeV for Model 1 (40 kyr) where radiative losses are balanced by the electron injection luminosity. The 36 kyr model has the same parameters as the 40 kyr model (see Table 2).



**Figure D1.** 21 kyr Model 1 as in Figure 4 but with 10% (grey shaded band) and 20% (pink shaded band) variation in parameters.



**Figure D2.** 40 kyr Model 2 as in Figure 5 but with 10% (grey shaded band) and 20% (pink shaded band) variation in parameters.  
MNRAS **000**, 1Doc-Start–20figure.caption.18 (2022)

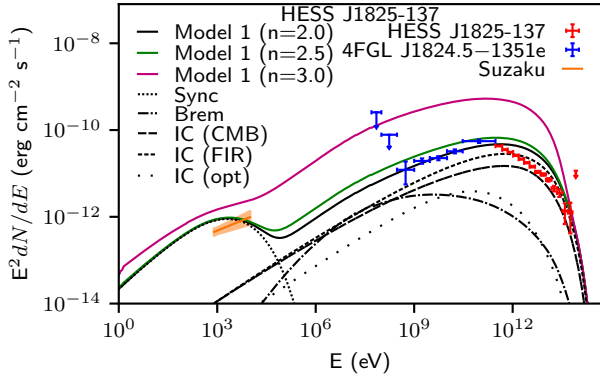


Figure E2: SED towards HESS J1825-137 for Model 1 (21 kyr,  $n = 2$ , black, see Table 2) vs Model 1 (21 kyr,  $n = 2.5$ , green) and Model 1 (21 kyr,  $n = 3$ , purple).

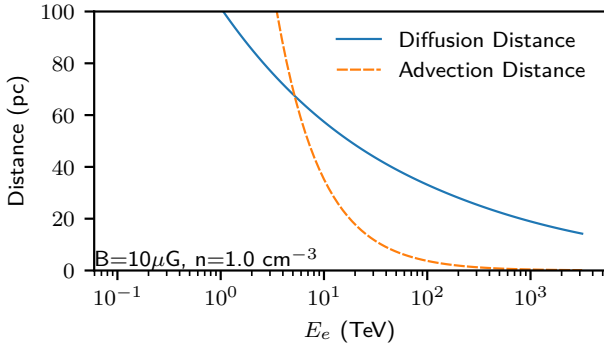
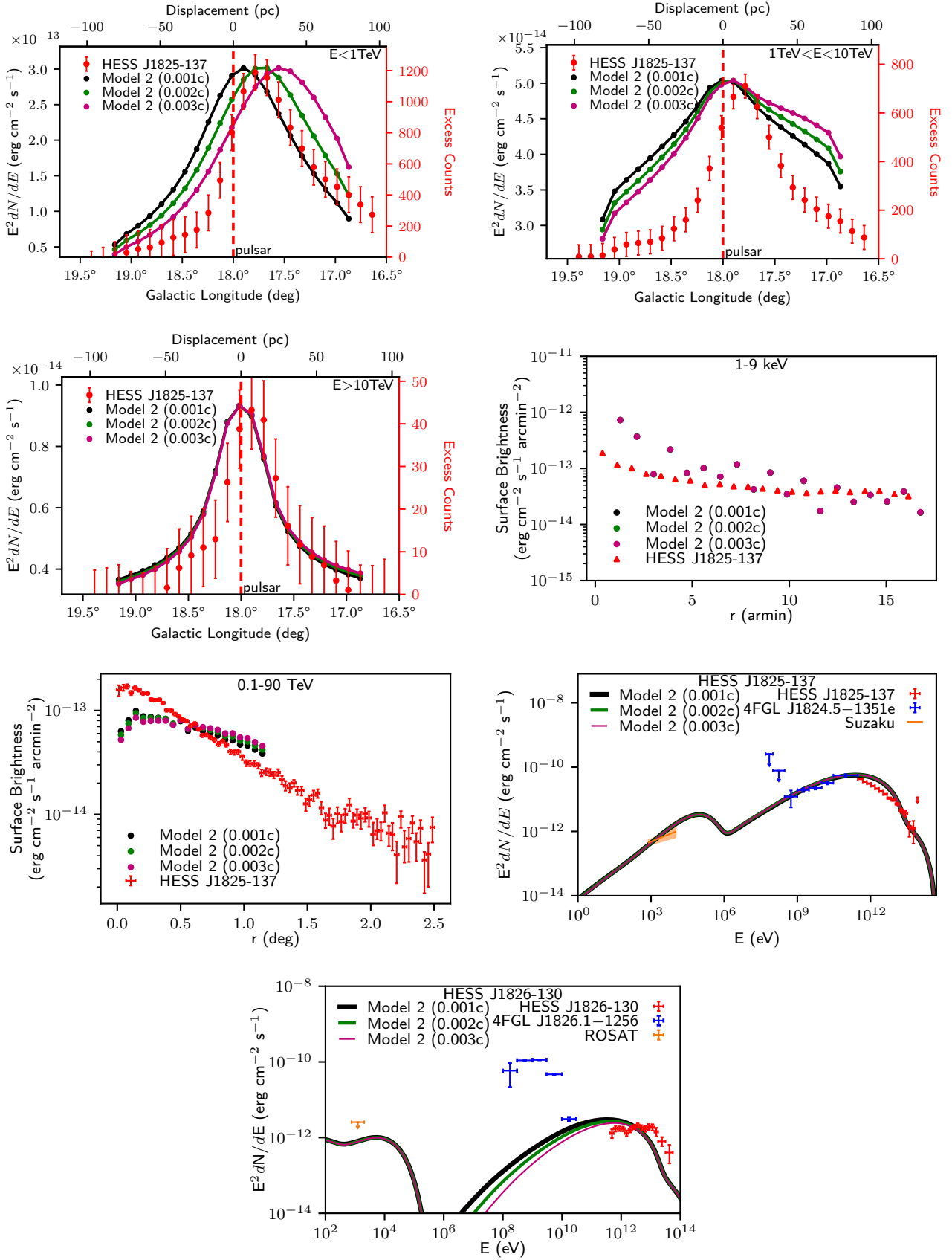


Figure E3: The distance that electrons are transported before losing their energy through radiative cooling (synchrotron, inverse Compton and Bremsstrahlung) assuming purely diffusive (solid line) or advective transport (dashed line).

This paper has been typeset from a  $\text{\LaTeX}$  file prepared by the author.





**Figure E4.** The slice profiles (top & top-middle left), surface brightness radial profiles (top-middle right & bottom-middle left) and SED towards HESS J1825-137 (bottom-middle right) and HESS J1826-130 (bottom) for Model 2 0.001c (black), 0.002c (green) and 0.003c (purple). See Table 2 for model parameters.